

A dark matter profile to model diverse feedback-induced core sizes of Λ CDM haloes

Alexandres Lazar^{1*}, James S. Bullock¹, Michael Boylan-Kolchin², T.K. Chan^{3,4}, Philip F. Hopkins⁵, Andrew S. Graus², Andrew Wetzel⁶, Kareem El-Badry⁷, Coral Wheeler⁴, Maria C. Straight^{8,2}, Dušan Kereš⁴, Claude-André Faucher-Giguère⁹, Alex Fitts² and Shea Garrison-Kimmel⁵

¹Department of Physics and Astronomy, University of California, Irvine, CA 92697 USA

²Department of Astronomy, The University of Texas at Austin, 2515 Speedway, Stop C1400, Austin, Texas 78712-1205, USA

³Institute for Computational Cosmology, Durham University, South Road, Durham, DH1 3LE, UK

⁴Department of Physics, Center for Astrophysics and Space Science, University of California at San Diego, 9500 Gilman Dr.

⁵California Institute of Technology, TAPIR, Mailcode 350-17, Pasadena, CA 91125, USA

⁶Department of Physics, University of California, Davis, CA 95616, USA

⁷Department of Astronomy and Theoretical Astrophysics Center, University of California Berkeley, Berkeley, CA 94720

⁸Department of Physics, Whitworth University, 300 West Hawthorne Road, Spokane, Washington 99251, USA

⁹Department of Physics and Astronomy and CIERA, Northwestern University, 2145 Sheridan Road, Evanston, IL 60208, USA

Working Draft

ABSTRACT

We analyze the cold dark matter density profiles of 54 galaxy halos simulated with FIRE-2 galaxy formation physics, each resolved within 0.5% of the halo virial radius. These halos contain galaxies with masses that range from ultra-faint dwarfs ($M_{\star} \simeq 10^{4.5} M_{\odot}$) to the largest spirals ($M_{\star} \simeq 10^{11} M_{\odot}$) and have density profiles that are both cored and cuspy. We characterize our results using a new, analytic density profile that extends the standard two-parameter Einasto form to allow for a pronounced constant-density core in the resolved innermost radius. With one additional core-radius parameter, r_c , this three-parameter *core-Einasto* profile is able to characterize our feedback-impacted dark matter halos more accurately than other three-parameter profiles proposed in the literature. In order to enable comparisons with observations, we provide fitting functions for r_c and other profile parameters as a function of both M_{\star} and $M_{\star}/M_{\text{halo}}$. In agreement with past studies, we find that dark matter core formation is most efficient at the characteristic stellar-mass to halo-mass ratio $M_{\star}/M_{\text{halo}} \simeq 5 \times 10^{-3}$, or $M_{\star} \sim 10^9 M_{\odot}$, with cores that are roughly the size of the galaxy half-light radius, $r_c \simeq 1 - 5$ kpc. Furthermore, we find no evidence for core formation at radii $\gtrsim 100$ pc in galaxies with $M_{\star}/M_{\text{halo}} < 5 \times 10^{-4}$ or $M_{\star} \lesssim 10^6 M_{\odot}$. For Milky Way-size galaxies, baryonic contraction often makes halos significantly more concentrated and dense at the stellar half-light radius than DMO runs. However, even at the Milky Way scale, FIRE-2 galaxy formation still produces small dark matter cores of $\simeq 0.5 - 2$ kpc in size. Recent evidence for a ~ 2 kpc core in the Milky Way’s dark matter halo is consistent with this expectation.

Key words: galaxies: evolution – galaxies: formation – dark matter

1 INTRODUCTION

The theory of Cold Dark Matter with the inclusion of the cosmological constant (Λ CDM) has been the benchmark paradigm in cosmological studies, as its framework has been successful in modeling the distribution of large-scale structure of our universe. However, on small scales, there are potential inconsistencies between predictions made by the Λ CDM paradigm and what is observed in real galaxies. One of these inconsistencies concerns the distribution of dark matter in centers of galaxies. This known as the *cuspy-core* problem: dark matter halos simulated without baryons in Λ CDM have *cusped* dark matter densities at small radii, i.e. $\rho(r) \propto r^{\alpha}$ with $\alpha \sim -1$ (Dubinski & Carlberg 1991; Navarro

et al. 1997, 2004), while observations of some dark matter dominated galaxies appear to suggest profiles are better described by constant-density *cores* at small radii, i.e. $\alpha \sim 0$ (Flores & Primack 1994; Moore 1994; Salucci & Burkert 2000; Swaters et al. 2003; Gentile et al. 2004; Spekkens et al. 2005; Walter et al. 2008; Oh et al. 2011; Relatores et al. 2019). Another potentially related discrepancy is called the *Too Big to Fail* problem (Boylan-Kolchin et al. 2011): Milky Way satellite galaxies are observed to have much smaller inner dark matter densities compared to the surplus of subhalos predicted from (dark matter only) cosmological N -body simulations. This problem also persists in other dwarf galaxies of the Local Group and local field (Garrison-Kimmel et al. 2014; Tollerud et al. 2014; Papastergis et al. 2015).

Most of the above-mentioned problems were posed from dark matter only simulations, which lack the effects of baryons. One way galaxy formation can affect dark mat-

* aalazar@uci.edu

ter is by boosting central dark matter densities as a result of baryons clustering at the center of the halo (Blumenthal et al. 1986). This denoted as “baryonic contraction” in the literature and it is an effect that is particularly important for Milky Way-mass galaxies (e.g. Gnedin et al. 2004; Chan et al. 2015). Alternatively, the inner dark matter density can decrease in response to repetitive energetic outflows from stellar feedback, a process often referred to as “feedback-induced core formation”, and one that is most effective in galaxies that are somewhat smaller than the Milky Way (Navarro et al. 1996; Read & Gilmore 2005; Governato et al. 2010, 2012; Pontzen & Governato 2012; Teyssier et al. 2013; Di Cintio et al. 2014a; Chan et al. 2015; Brook & Di Cintio 2015; Tollet et al. 2016). Another possibility is that dynamical friction from small accretion events (El-Zant et al. 2001; Tonini et al. 2006; Romano-Díaz et al. 2008; Goerdt et al. 2010; Cole et al. 2011) can flatten the dark matter density profile.

The effects of feedback on core formation depend sensitively on the total amount and precise nature of star formation. For example, Peñarrubia et al. (2012) showed that galaxies with too few stars (and therefore, too few supernovae) are unlikely to have feedback-induced cores owing to an insufficient amount energy from supernovae to substantially transform the dark matter profile. Mashchenko et al. (2006) showed that concentrated star formation episodes that are *spatially* displaced from halo centers can drive bulk gas flows, alter dark matter particle orbits, and increase the likelihood for dark matter core formation. Time-repetitive “bursty” star formation also affects core formation, allowing for dark matter particle orbits to be affected significantly over time as gas is expelled and re-accreted in the baryon cycle (Pontzen & Governato 2012). The timing of star formation relative to dark matter halo growth can also affect core formation; in cases where dark matter rich mergers occur after core-producing star formation, cusps can be reborn (Oñorbe et al. 2015). Dark matter core formation is seen in many fully self-consistent cosmological simulations that resolve star formation on small spatial scales (e.g. Governato et al. 2010; Munshi et al. 2013; Brooks & Zolotov 2014; Madau et al. 2014; Oñorbe et al. 2015; El-Badry et al. 2016; Tollet et al. 2016; Fitts et al. 2017). One common aspect of these simulations is that they have relatively high gas density thresholds for star formation. Cosmological simulations with lower density thresholds for star formation, e.g. APOSTLE and Auriga (Bose et al. 2019), have been shown to not produce dark matter cores. The dependence of feedback-induced core formation on the star formation density threshold has been studied in more detail by Dutton et al. (2019) and Benítez-Llambay et al. (2019). Both concluded that density thresholds higher than the mean ISM density, which allows for some ISM phase structure and clustered star formation as observed, is necessary in forming feedback-induced cores.

Di Cintio et al. (2014a) studied the relationship between the inner local density slope of dark matter, α , and the stellar mass fraction, M_\star/M_{halo} , of simulated galaxies from the MUGS (Stinson et al. 2010) and MaGICC (Brook et al. 2012; Stinson et al. 2012) simulations for a wide range stellar mass systems, $M_\star \approx 10^{5-11} M_\odot$. They found that core formation is a strong function the mass-ratio of stars formed to total halo mass and demonstrated that there is a characteristic mass-

ratio for efficient core formation $M_\star/M_{\text{halo}} \approx 5 \times 10^{-3}$, above and below which galaxy halos approach the cuspy behavior associated with dark matter only simulations. Chan et al. (2015) used galaxies of stellar masses, $M_\star = 10^{3-11} M_\odot$, from the FIRE-1 suite (Hopkins et al. 2014) to study feedback-induced core formation and found similar results. Tollet et al. (2016) used the NIHAO suite (Wang et al. 2015) for a wide range of halo masses, $M_{\text{halo}} = 10^{10-12} M_\odot$ and further confirmed this qualitative phenomena. Recently, Macciò et al. (2020) extended the work of Tollet et al. (2016) with the inclusion of black hole feedback for galaxies spanning eight orders in magnitude in stellar mass.

The above-mentioned simulation groups agree on a few additional qualitative points. First, feedback typically does not produce significant deviations from cuspy dark matter only predictions in the smallest galaxies: $M_\star/M_{\text{halo}} < 10^{-4}$ ($M_\star \lesssim 10^6 M_\odot$, typically), as expected on energetic grounds (Peñarrubia et al. 2012; Garrison-Kimmel et al. 2013). Second, dark matter halos become more cored as M_\star/M_{halo} increases up until $M_\star/M_{\text{halo}} \approx 5 \times 10^{-3}$, which is the region of *peak* core formation. These halos are not well modeled by cuspy density profiles and must be described by an alternative dark matter profile that has a pronounced flattening in slope at small radii. In higher mass halos, $M_{\text{halo}} \approx 10^{12} M_\odot$, baryonic contraction actually makes halos denser at the stellar half-mass radius than dark matter only simulations would suggest. However, Chan et al. (2015) found that within this radius, small cores are often present even within baryonically-contracted $10^{12} M_\odot$ halos.

The analysis done in Di Cintio et al. (2014b) explored a general five-parameter density profile to characterize halos with either cuspy or cored inner density profiles. In addition to a characteristic radius and density, this profile had three shape parameters: α , β , and γ (Zhao 1996). They found that the values of the three shape parameters varied regularly as a function of the M_\star/M_{halo} and provided fitting functions that captured these trends. Therefore, given M_\star/M_{halo} , the Di Cintio et al. (2014b) profile reduces to a two free-parameter function that may be used to compare predictions with observations in a fairly straightforward manner.

The $\alpha\beta\gamma$ -profile can be regarded as a generalization of the Navarro et al. (1997, NFW) profile, which provides a good fit to dark matter only simulations. Since dark matter only simulations have traditionally been characterized by the NFW profile, there have been attempts to modify the NFW form by allowing for a constant density core radius parameter $r_c \equiv r_{\text{core}}$. For example, Peñarrubia et al. (2012) suggested a three-parameter core profile: the classic NFW profile with a core radius in the inner radial regions of the halo. Read et al. (2016) derives a core profile starting with an NFW form by connecting core formation to features of star-formation efficiency and the stellar half-mass radius. More recently, Freundlich et al. (2020) used NIHAO to explore a constrained version of the $\alpha\beta\gamma$ profile that has three-parameters, the “Dekel+” profile (Dekel et al. 2017), with a variable inner slope and concentration parameter.

In what follows, we revisit the question of dark matter halo density profiles in cosmological galaxy formation simulations using the FIRE-2 feedback model (Hopkins et al. 2018). The simulations we consider herein allow us to resolve to within 0.5% of the halo virial radius in halos that produce galaxies spanning six orders of magnitude in stellar mass. We

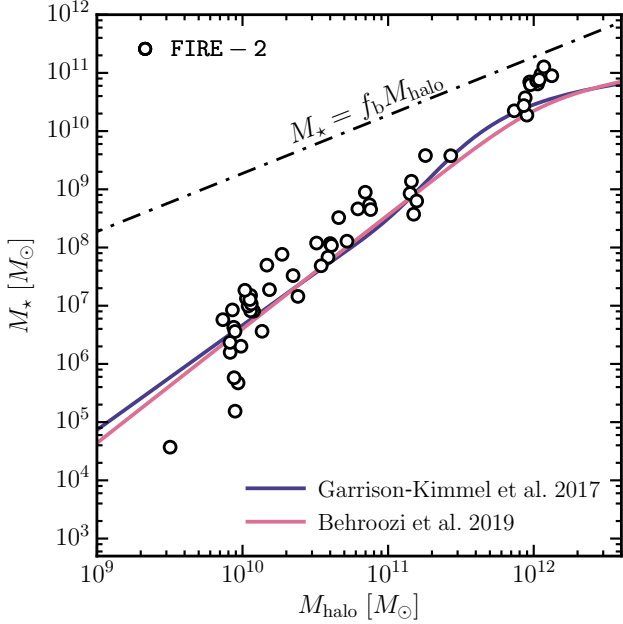


Figure 1. — *Stellar mass to halo mass relations.* The white points show galaxies from the FIRE-2 simulations studied in this paper. The curves are the median abundance matching relations presented in (Garrison-Kimmel et al. 2017, zero scatter) (blue) and Behroozi et al. (2019) (pink).

introduce a new analytic density profile, the “core-Einasto”, that extends the Einasto (1965) form by adding one free parameter, a physical core radius, r_c . It is well known that the two-parameter Einasto profile provides a better fit to dark matter only simulations than the two-parameter NFW (Navarro et al. 2004; Wang et al. 2019). Similarly we find that the three-parameter core-Einasto profile provides a better fit to FIRE-2 halos than two popular three-parameter versions of generalized double-power law profiles: the Dekel+ profile (Dekel et al. 2017; Freundlich et al. 2020) and a cored extension of the NFW (Peñarrubia et al. 2012). We also find that the two-parameter Di Cintio et al. (2014b) profile is not a good fit to our feedback-affected halos.

In addition to providing a better fit to our FIRE-2 halos than other three-parameter profiles, the core-Einasto profile utilizes a physically-meaningful core-radius parameter, r_c . The numerical value of r_c matches well to the radius where a visual profile begins to flatten towards a constant density. The combination of accuracy, intuitive parameters, and ease-of-use will hopefully allow our three-parameter core-Einasto profile to become a useful tool for comparing predictions to observations.

This article is structured as follows: Section 2 discusses our sample of high resolution galaxies simulated with FIRE-2 physics along with their relevant properties. We also discuss the numerical intricacies considered for our galaxies. Section 3 revisits the analysis of correlations between α and M_*/M_{halo} for our sample of galaxies and dark matter halos. In Section 4, we introduce the cored version of the classic Einasto profile used to model Λ CDM halos. We use the properties of these profiles to provide constraints on dark matter cores as a function and of M_*/M_{halo} . We summarize our results and discuss potential uses for observational

and cosmological studies in Section 5. The appendix includes five sections: **A** has expressions for fitting parameters as a function of stellar mass; **B** derives analytical expressions for the mass and gravitational potential implied by the core-Einasto profile; **C** has a four-parameter core-Einasto extension that better accounts for adiabatic contraction in Milky Way size halos; **D** presents comparisons to fits with alternative three-parameter profiles and also presents fits for the five-parameter $\alpha\beta\gamma$ form; and **E** provides tables that list all halo properties and best-fit profile parameters for each halo in our sample.

2 NUMERICAL METHODOLOGY

In this section, we briefly describe the suite of high-resolution simulations used in our analysis. We discuss the FIRE-2 model for full galaxy formation physics in Section 2.1, the numerical parameters used in our high resolution simulations in Sections 2.2 and 2.5, and present the halo sample used in this analysis in Section 2.3. The numerical simulations presented here are all part of the Feedback In Realistic Environments (FIRE) project¹ and are listed in Table E1 at the end of this article.

2.1 The FIRE-2 model

Our simulations were run using the multi-method code GIZMO (Hopkins 2015), with the second-order mesh-free Lagrangian-Godunov finite mass (MFM) method for hydrodynamics. GIZMO utilizes an updated version of the PM+Tree algorithm from GADGET-3 (Springel 2005) to calculate gravity and adopts fully conservative adaptive gravitational softening for gas (Price & Monaghan 2007). The FIRE-2 model (Hopkins et al. 2018), which is an updated version of the FIRE-1 feedback scheme from Hopkins et al. (2014), is used to implement star formation and stellar feedback physics. Gas and gravitational physics implemented are discussed in complete detail in Hopkins et al. (2018). Here we discuss in brief detail the feedback physics relevant to core formation.

The simulations presented here tabulate the relevant ionization states and cooling rates from a compilation of CLOUDY runs (Ferland et al. 1998), accounting for gas self-shielding. The gas cooling mechanisms follow the cooling rates of $T = 10 - 10^{10}$ K; these include metallicity-dependent fine-structure atomic cooling, low temperature molecular cooling, and high temperature metal-line cooling that followed 11 separately tracked species. Gas is heated and ionized throughout cosmic time using the redshift dependent UV background model from Faucher-Giguère et al. (2009) that ionizes and heats gas in an optically thin approximation and uses an approximate prescription to account for self-shielding of dense gas using a Sobolev/Jeans-length approximation. Stars are formed in Jeans-unstable, molecular gas regions at densities $n_{\text{H}} \geq 10^3 \text{ cm}^{-3}$, with 100% instantaneous efficiency per local free-fall time in dense gas. Each star particle is an assumed stellar population with a Kroupa (2001) IMF that inherits its metallicity from its parent gas particle

¹ The FIRE project website: <http://fire.northwestern.edu>

and has an age determined by its formation time. The stellar feedback implemented includes stellar winds, radiation pressure from young stars, Type II and Type Ia supernovae, photoelectric heating, and photo-heating from ionizing radiation. Feedback event rates, luminosities, energies, mass-loss rates, and other quantities are tabulated directly from stellar evolution models (STARBURST99 ; [Leitherer et al. 1999](#)).

2.2 Numerical simulations

All simulations in this analysis use a zoom-in technique ([Oñorbe et al. 2014](#)) to reach high resolutions in a cosmological environment by constructing a convex-hull region and refining it in progressively higher-resolution shells until the desired resolution is reached in the inner-most region. All initial conditions are generated with MUSIC ([Hahn & Abel 2011](#)) and then the simulations are evolved from redshifts $z \approx 100$ to $z = 0$ assuming a flat Λ CDM cosmology. We note that the cosmological parameters in each of the simulations vary to some degree, but remain consistent with [Planck Collaboration et al. \(2016\)](#). Across our entire simulation sample: $h = 0.68 - 0.71$, $\Omega_\Lambda = 1 - \Omega_m = 0.69 - 0.73$, $\Omega_b = 0.0455 - 0.048$, $\sigma_8 = 0.801 - 0.82$, $n_s = 0.961 - 0.97$. In post-processing, halos are identified using the phase-space halo finder ROCKSTAR ([Behroozi et al. 2013](#)), which uses adaptive, hierarchical refinement of the friends-of-friends groups in 6-dimensional phase-space and one time dimension. This results in robust tracking of halos and subhalos ([Srisawat et al. 2013](#)).

2.3 Halo sample & nomenclature

Throughout this paper, dark matter halos are defined as spherical systems with virial radius, r_{vir} , inside of which the average density is equal to $\Delta_{\text{vir}}(z)\rho_{\text{crit}}(z)$. Here, $\rho_{\text{crit}}(z) := 3H^2(z)/8\pi G$ is the critical density of the universe and $\Delta_{\text{vir}}(z)$ is the redshift evolving virial overdensity defined in [Bryan & Norman \(1998\)](#). The virial mass of a dark matter halo, denoted by M_{halo} , is then defined as the dark matter mass within r_{vir} . The stellar mass of the galaxy, M_\star , is then taken to be the total sum of the stellar particles inside $10\% \times r_{\text{vir}}$. It follows that the three-dimensional stellar-half-mass radius, $r_{1/2}$, is the radius that encloses half of the defined stellar mass. Finally we refer to the “stellar fraction” of the halo as the ratio between the quantified stellar mass and the halo mass: M_\star/M_{halo} .

[Fig. 1](#) outlines our sample of galaxies, where just the dark matter halo masses (from the FIRE-2 runs) are plotted against M_\star . We compare our sample with the abundance matching relations presented in ([Garrison-Kimmel et al. 2017](#), zero scatter) and [Behroozi et al. \(2019\)](#) as the blue and pink curves, respectively, showing the best fit median abundance matching relations. [Table E1](#) lists all of the halos galaxies in this paper, including their $z = 0$ properties from the FIRE-2 runs. Given our large sample, we chose to divide our galaxy sample into four convenient classifications of objects using the convention from [Bullock & Boylan-Kolchin \(2017\)](#):²

Ultra-Faint Dwarfs: Defined to have stellar masses of $M_\star \approx 10^{2-5} M_\odot$ at $z = 0$. These are analogs of galaxies to be detected within limited local volumes around M31 and the Milky Way.

Classical Dwarfs: Defined to have stellar masses of $M_\star \approx 10^{5-7} M_\odot$ at $z = 0$. These are analogs of the faintest galaxies known prior to *SDSS*.

Bright Dwarfs: Defined to have stellar masses of $M_\star \approx 10^{7-10} M_\odot$ at $z = 0$. These are analogs of the faintest galaxies that can be seen in wide-field galaxy surveys.

Milky Way-Mass Halos: Defined to host spiral galaxies with stellar mass of $M_\star \approx 10^{10-11} M_\odot$ at $z = 0$. At the peak of abundance-matching relation, this maps to the generally accepted range in Milky Way-mass halos of $M_{\text{halo}} = [0.8 - 2.4] \times 10^{12}$. Hereafter, we abbreviate Milky Way as “MW”.

Lastly, each zoomed-in halo run with full FIRE-2 physics has an analogous dark matter only (DMO) version. The individual dark matter particle masses in the DMO versions are larger by a factor of $(1 - f_b)^{-1}$ in these runs, where $f_b := \Omega_b/\Omega_m$ is the cosmic baryon fraction, but the initial conditions are otherwise identical. The density profiles quoted from the DMO simulations have been scaled $m_p \rightarrow (1 - f_b)m_p$ in order to roughly account for the exclusion of the baryons. Other quantities are also adjusted accordingly: $\rho(r) \rightarrow (1 - f_b)\rho(r)$, $M_{\text{halo}}(< r) \rightarrow (1 - f_b)M_{\text{halo}}(< r)$ and $V_{\text{circ}}(r) \rightarrow \sqrt{1 - f_b}V_{\text{circ}}(r)$, for all of the results analyzed in the DMO runs. This provides a simple comparison set to understand the additional effects of energetic feedback seen in our FIRE-2 runs.

2.4 Radial profiles

For each main halo identified by ROCKSTAR, the center of the halo is quantified through a “shrinking spheres” iteration scheme ([Power et al. 2003](#); [Navarro et al. 2004](#)): the center of mass of particles is computed in a sphere and then has its radius reduced by half and re-centered on the new center of mass. This is done successively until the sphere contains one thousand particles. The final center of mass position is determined at this last iteration. For our galaxies, this is done for the combined star and dark matter particles found inside the virial radius while the center of mass for the DMO analogs are done with only dark matter inside the halo.³ The spherically averaged local density profile, $\rho(r)$, is constructed in 35 logarithmically spaced bins over $[0.005 - 1] \times r_{\text{vir}}$. We expect systematic uncertainties in the binned density estimates to be extremely minimal due to large number of particles in each simulation sample. Throughout the entirety of this paper, we refer to these local density profiles as the density profiles for the dark matter halo.

2.5 Region of numerical convergence

We expect the innermost regions of our simulated halos to be affected by numerical relaxation. With a variety of galaxies

² Note that these classifications are based on galaxies that span specific stellar mass ranges.

³ We also compared our results with centers defined as the most bound dark matter particle in the halo determined by ROCKSTAR. We find no qualitative differences in our final results.

simulated at different resolutions, we must account for resolution differently in each simulation. We do so using the method specified in Power et al. (2003), where the effective resolution of cosmological simulations is related to the radius where the two-body relaxation timescale, t_{relax} , becomes shorter than the age of the universe, t_0 . Precisely, the radius at which numerical convergence is achieved, r_{conv} , is dependent on the number of enclosed particles, $N(< r)$, as well as the mean density enclosed at the associated radius, $\bar{\rho}(r) = 3M(< r)/4\pi r^3$, where $M(< r)$ is the total mass contained within radius r . Therefore, r_{conv} is governed by the following equation:

$$\frac{t_{\text{relax}}(r)}{t_0} = \frac{\sqrt{200}}{8} \frac{N}{\ln N} \left[\frac{\bar{\rho}(r)}{\rho_{\text{crit}}} \right]^{-1/2}. \quad (1)$$

A rigorous study of the numerical convergence for DMO halos and the FIRE-2 galaxies (dark matter with baryons) has been discussed in detail in Hopkins et al. (2018). There, the convergence has been gauged as a function of mass resolution, force resolution, time resolution, and so on.

For the DMO simulations, convergence was shown to be well resolved to the radius at which the criterion satisfies $t_{\text{relax}} > 0.6 t_0$ with $< 1\%$ resolution level deviations. This typically equates to ~ 2000 particles and is more conservative for the ranges of resolution levels analyzed in our halo sample. However, even at ~ 200 particles (resulting in a factor ~ 2 smaller radius of convergence), the convergence is good to $\sim 10\%$ in the density profile. Hereafter, we adopt $t_{\text{relax}} = 0.6 t_0$ as our resolution criterion to maintain consistency across all of our simulations. We define $r_{\text{conv}} := r_{0.6}^{\text{DM}}$ to be the radius at which the resolution criterion is fulfilled for the *dark matter only* analogs of each sample halo, meaning that $r > r_{\text{conv}}$ is our best estimate of the numerically converged region. In Hopkins et al. (2018), convergence for simulations ran with baryons can be much better or worse in comparison to their DMO analogs, but convergence is entirely dominated by the convergence from the baryons. So in the context of our galaxies, the criterion of convergence has much more to do with the star-formation dynamics and converging baryonic physics rather than having to do with the number of particles enclosing a specific region. With this, r_{conv} from the DMO analogs are applied to the galaxies of the FIRE-2 halos throughout this paper as a conservative estimate. For more details regarding the numerical convergence study of FIRE-2 halos, we refer to Hopkins et al. (2018).

3 STELLAR FRACTION RELATION WITH THE INNER-DENSITY SLOPE

We begin by comparing our catalog of galaxies with previous results in the literature. The stellar mass fraction, which we define as the ratio between the stellar mass and halo mass, $M_{\star}/M_{\text{halo}}$, has a relationship with the slope of the dark matter density profile found at the innermost radii (Di Cintio et al. 2014a; Chan et al. 2015; Tollet et al. 2016). Following the convention of Di Cintio et al. (2014a), the effect of feedback on the inner dark matter halo density can be captured by exploring the best-fitting power law for the dark matter density profile over a specific radial range, $\rho(r) \propto r^{\alpha}$. Di Cintio et al. (2014a) suggested using α fitted over the radial range $r \in [1 - 2\% r_{\text{vir}}]$ since the lower limit of

$1\% r_{\text{vir}}$ satisfied the Power et al. (2003) radius criterion of convergence for the majority of their halo sample.

Fig. 2 summarizes the relation between α and the stellar mass fraction at $z = 0$ for our simulations and compares to results from (Di Cintio et al. 2014a, green band) and (Tollet et al. 2016, blue band). The analysis performed in (Di Cintio et al. 2014a, green) included only stellar mass fractions down to $M_{\star}/M_{\text{halo}} \simeq 4 \times 10^{-5}$, so we restrict their curve to that limit. The differences between the two curves included differences in cosmological models used, as noted in (Tollet et al. 2016). The black filled circles are our simulated FIRE-2 galaxies and the black open circles are the results for the DMO simulations (for which we use the stellar mass of their galaxy analogs). For all values of $M_{\star}/M_{\text{halo}}$, the DMO analogs are cuspy, with $\alpha \approx -1.5$, which is expected when assuming the behavior of an analytic NFW profile along with scatter induced by the mass-concentration relation (see Bullock & Boylan-Kolchin 2017).

The pink band captures our results using the fitting-formula shape suggested by Tollet et al. (2016):

$$\alpha(x) = n - \log_{10} \left[n_1 \left(1 + \frac{x}{x_1} \right)^{-\beta} + \left(\frac{x}{x_0} \right)^{\gamma} \right], \quad (2)$$

where $x = M_{\star}/M_{\text{halo}}$. We find that $n = -1.60$, $n_1 = 0.80$, $x_0 = 9.18 \times 10^{-2}$, $x_1 = 6.54 \times 10^{-3}$, $\beta = 5$, and $\gamma = 1.05$ matches our results in the median. The general purpose of this fit is to guide the eye. We also binned by $M_{\star}/M_{\text{halo}}$ to compute a rough estimate of the standard deviation found at each stellar fraction. The width of the pink band roughly corresponds to the 1σ dispersion about the median. The width of the green and blue bands are set at a constant $\Delta\alpha = \pm 0.2$.

Ultra-faint and classical dwarf galaxies, with low stellar mass fractions of $M_{\star}/M_{\text{halo}} \lesssim 10^{-3}$, have inner densities slopes of $\alpha \approx -1.5$, the same as their DMO analogs. From there and increasing to $M_{\star}/M_{\text{halo}} \simeq 5 \times 10^{-3}$, the inner dark matter densities of the bright dwarf galaxies transition to more cored profiles. At $M_{\star}/M_{\text{halo}} \simeq 5 \times 10^{-3}$, our galaxies reach efficient core formation (shown more directly below), with $\alpha \approx -0.25$. The diversity in core strength, as quantified by α , is largest from $M_{\star}/M_{\text{halo}} \approx 10^{-3}$ to 5×10^{-3} , with a variance of $\Delta\alpha \approx \pm 0.35$ about the median. Note that one bright dwarf (m11q) at $M_{\star}/M_{\text{halo}} \simeq 4 \times 10^{-3}$ has what appears to be a cuspy central density. We checked the assembly history of this galaxy and verified that it is not particularly unusual, with its last major merger at $z \sim 2$. This galaxy does in fact have a constant density core (see Table E2 in the appendix), but at a radius ~ 850 pc, which is smaller than $1\% r_{\text{vir}} \sim 1500$ pc, meaning that it is not detected using this α slope measurement. From the region of efficient core formation to MW masses, α decreases. The scatter in α remains large ($\Delta\alpha \approx \pm 0.3$) until $M_{\star}/M_{\text{halo}} \approx 6 \times 10^{-2}$, which is in the range of the majority of the MW-mass halos. The scatter is minimized at $\Delta\alpha \approx \pm 0.15$ for these galaxy masses.

Our findings agree with previous results in the literature for the region of efficiently peaked core formation: $M_{\star}/M_{\text{halo}} \simeq 5 \times 10^{-3}$ (Di Cintio et al. 2014a; Chan et al. 2015; Tollet et al. 2016). While we do not have a significant sample of ultra-faint dwarfs, we find negligible core formation for $M_{\star}/M_{\text{halo}} \lesssim 10^{-4}$. The most significant difference we see with past results are (i) core formation that is less pronounced than previously reported for $M_{\star}/M_{\text{halo}} \simeq 10^{-3}$

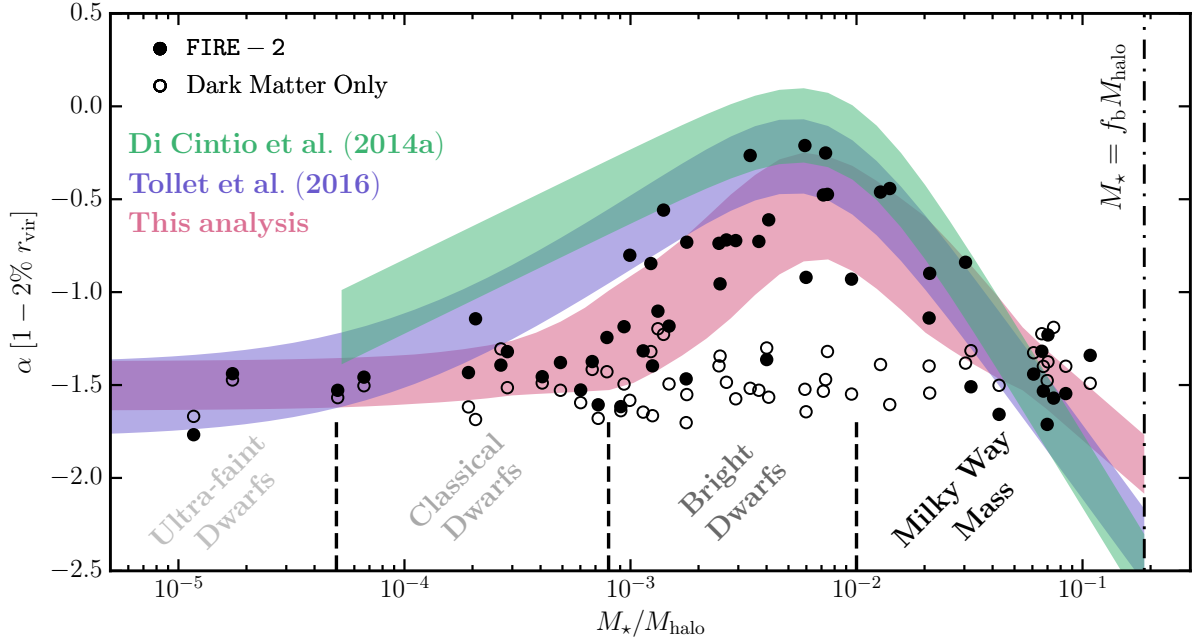


Figure 2. — *The impact of feedback physics on the inner dark matter densities.* Shown is the inner dark matter density slope, α , averaged over $[1 - 2\%] \times r_{\text{vir}}$, as function of the stellar mass fraction, $M_{\star}/M_{\text{halo}}$, at $z = 0$. Cored profiles have $\alpha \sim 0$, while cuspy inner density profiles have lower values of $\alpha \lesssim -1$. The open circles are the DMO analogs, which all have $\alpha \approx -1.5$ as expected from a NFW profile. The pink shaded region shows the 1σ dispersion about the smoothed binned median. As a comparison, the fits from (Di Cintio et al. 2014a, green) and (Tollet et al. 2016, blue) are also plotted using a constant width of $\Delta\alpha = \pm 0.2$ relative to the mean relation (Tollet et al. 2016). The curve from Di Cintio et al. (2014a) was only fitted to down to a stellar mass fraction of $M_{\star}/M_{\text{halo}} \approx 4 \times 10^{-5}$, so we restrict the curve to that mass limit

. The dispersion in α increases from the stellar mass fraction from $M_{\star}/M_{\text{halo}} \gtrsim 10^{-4}$, the regime of classical dwarfs and the brightest dwarfs, to the MW-mass halos with $M_{\star}/M_{\text{halo}} \approx 10^{-1}$. Feedback-induced core formation peaks at $M_{\star}/M_{\text{halo}} \approx 5 \times 10^{-3}$, the regime of the brightest dwarfs. At $M_{\star}/M_{\text{halo}} \lesssim 10^{-4}$, the regime of classical dwarfs and ultra-faints, the impact of stellar feedback is negligible.

($M_{\star} \approx 10^7 M_{\odot}$) and (ii) more scatter in α within the regime of the brightest dwarfs, with α ranging from quite cuspy ($\alpha \approx -1.5$) to very cored ($\alpha \approx -0.25$) over the small range $M_{\star}/M_{\text{halo}} \approx [2 - 5] \times 10^{-3}$.

While results on α at $r \approx 1.5\% r_{\text{vir}}$ have proven useful for characterizing the effectiveness of core formation as a function of stellar mass fraction in dark matter halos in the past, more recent simulations have allowed predictions at even smaller radii. This can potentially lead to small cores being unaccounted for (see Chan et al. 2015; Wheeler et al. 2019). For example, while Fig. 2 gives the impression that MW-mass halos will have density structure similar to the DMO (NFW-like) expectation, this is only because the log-slope at $[1 - 2\%]r_{\text{vir}}$ does not provide a complete picture. That is, while the log-slope at this radius is similar to that expected in the absence of galaxy formation, the overall density amplitude at $\sim 1\%$ of the virial radius is higher. In fact, as we will see in the upcoming section, at even smaller radii, our MW-mass halos have cored density profiles.⁴ This motivates a more complete examination into the shapes of profiles of simulated galaxy halos.

⁴ Also seen from the implementation of FIRE-1 physics for MW-mass halos in Chan et al. (2015).

4 A DENSITY PROFILE FOR FEEDBACK-AFFECTED HALOS

In this section, we present a new dark matter density profile that allows for constant-density cores of the type seen in our simulated galaxy halos. The new profile generalizes the Einasto (1965) profile, which has proven to be an excellent fit for halos formed in DMO simulations. Our “core-Einasto” (cEinasto) profile extends its behaviour with one free parameter — a core radius, r_c . After demonstrating that this profile does sufficiently well of capturing the density structure for a majority of the FIRE-2 halos, we follow the methodology employed in Di Cintio et al. (2014b), and provide fits for halo fitting parameters as functions of $M_{\star}/M_{\text{halo}}$ at $z = 0$. In Appendix A we provide profile parametrization as a function of galaxy stellar mass, M_{\star} . We note that in the course of this analysis, we explored several different options for analytic cored profiles and found that the core-Einasto form was the best of these fits. In Appendix D we show an example comparison between the core-Einasto profile and the Peñarrubia et al. (2012) (core-NFW) profile and demonstrate that core-Einasto provides a superior fit with the same number of free parameters.

4.1 Profiles for dark matter only halos

Dark matter halos in Λ CDM are fairly well-described by the Navarro-Frank-White (Navarro et al. 1997, NFW) double-

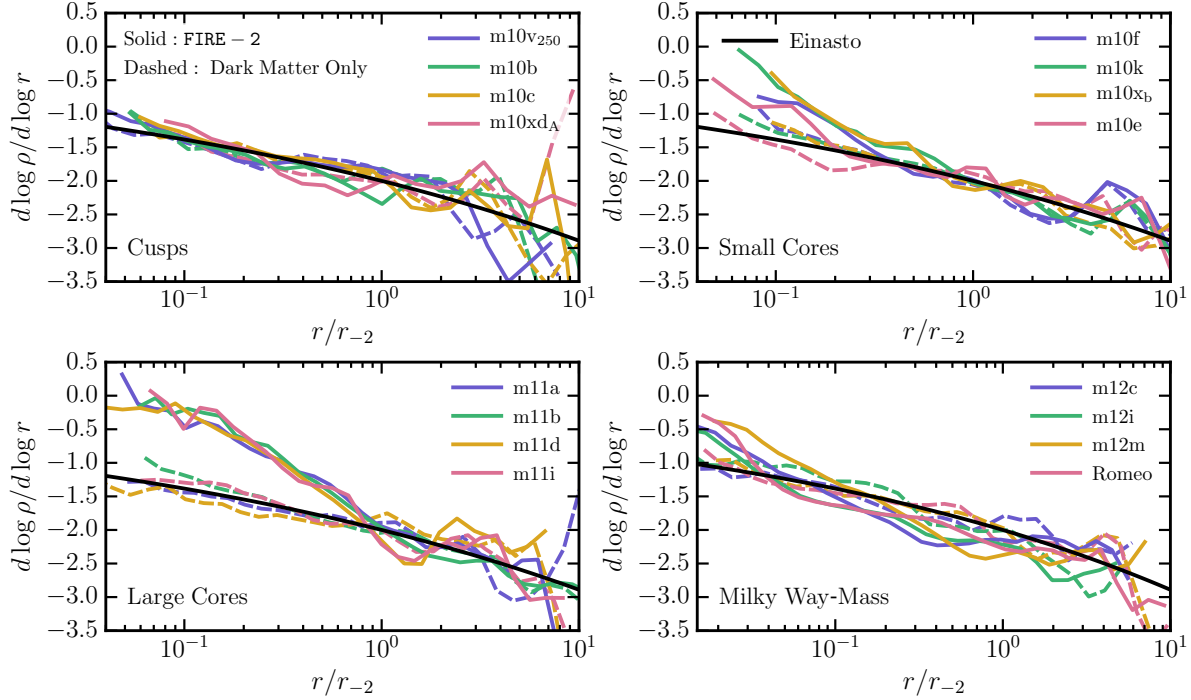


Figure 3. — *Comparison of the log-slope behaviour.* The four panels show galaxies grouped by the behavior of their inner density profiles: galaxies with cusps, small cores, large cores, and MW-mass halos. The resolved portions of the FIRE-2 galaxies are depicted as the solid lines while the resolved DMO analog profiles are plotted as dashed lines. The solid black line illustrates the slope expected from Eq. (3). All of the radial values are normalized by r_{-2} of the DMO analogs, which are computed by fitting Eq. (4) to each individual dashed curves. As expected, the galaxies with cusps are well described by Eq. (4). Galaxies with small cores have profiles that start to rise very slowly towards $d \log \rho / d \log r = 0$ at $\sim r_{-2}$. The largest cores in our sample are seen to have slight excesses in the density at around r_{-2} (the “dip” in the profile) and begins to rise substantially for decreasing values of r . Milky-Way mass halos are the outliers in the trend, in which the galaxies’ log-slopes are inconsistent with their dark matter analogs beginning at r_{-2} . At radii $r \ll r_{-2}$, the log-slopes are shown to form cores abruptly.

power law profile. While power laws are robust for understanding and are analytically friendly to work with, it has been made apparent that dark matter density profiles are not perfectly captured by the power-law construction. Navarro et al. (2004, 2010) demonstrated that higher resolution dark matter density profiles have log-slopes⁵ that decrease monotonically as r approaches the center, which is not captured by the NFW at small r . This indicates that the innermost regions of CDM halos are shallower than an NFW. Their study suggested a different radial profile for DMO halos, starting with the log-slope relation:

$$\frac{d \log \rho}{d \log r}(r) = -2 \left(\frac{r}{r_{-2}} \right)^{\alpha_\epsilon}. \quad (3)$$

This results in the three-parameter Einasto profile

$$\log \left[\frac{\rho_{\text{Ein}}(r)}{\rho_{-2}} \right] = -\frac{2}{\alpha_\epsilon} \left[\left(\frac{r}{r_{-2}} \right)^{\alpha_\epsilon} - 1 \right], \quad (4)$$

where α_ϵ is the so-called *shape parameter* that tunes how slow or fast the slope changes with radius, and r_{-2} (as well as $\rho_{-2} := \rho(r_{-2})$) is the radius (density) at which the logarithmic slope of the density profile is equal to -2 , i.e. $d \log \rho / d \log r|_{r=r_{-2}} = -2$.

⁵ We refer “log-slope” as the logarithmic derivative of the local density profile: $d \log \rho / d \log r$.

The shape parameter, α_ϵ , is a key component of Eq. (4). When obtained from Einasto profile fits to dark matter halos of cosmological simulations, it has been shown to correlate with the overdensity peak height of the dark matter halo and is calibrated based on the cosmology (e.g. Gao et al. 2008; Dutton & Macciò 2014; Klypin et al. 2016). Fixing $\alpha_\epsilon \simeq 0.16$ has been shown to provide a good fit for DMO halos throughout the literature (Prada et al. 2006; Merritt et al. 2006; Gao et al. 2008). With this choice, ρ_{Ein} becomes a two-parameter function, one that still provides a better fit to DMO simulations than the two-parameter NFW profile.⁶ Recently, Wang et al. (2019) have shown that the two-parameter version of ρ_{Ein} provides an adequate fit for DMO halos over 30 orders of magnitude in halo mass. We fix $\alpha_\epsilon = 0.16$ in what follows.

4.2 Cored profile for feedback-affected CDM halos

We follow Navarro et al. (2004) and consider the behaviour of the log-slope of the density profiles for our galaxy halos as a function of radius. Fig. 3 shows log-slope profiles for

⁶ Of course, one can acquire even better density profile fits as good as 5–10% for halos in our mass range when leaving α_ϵ as a free parameter, as this value tailors to each shape to the dark matter halo. This however, leaves ambiguity in the value of r_{-2} , as this is now dependent on α_ϵ .

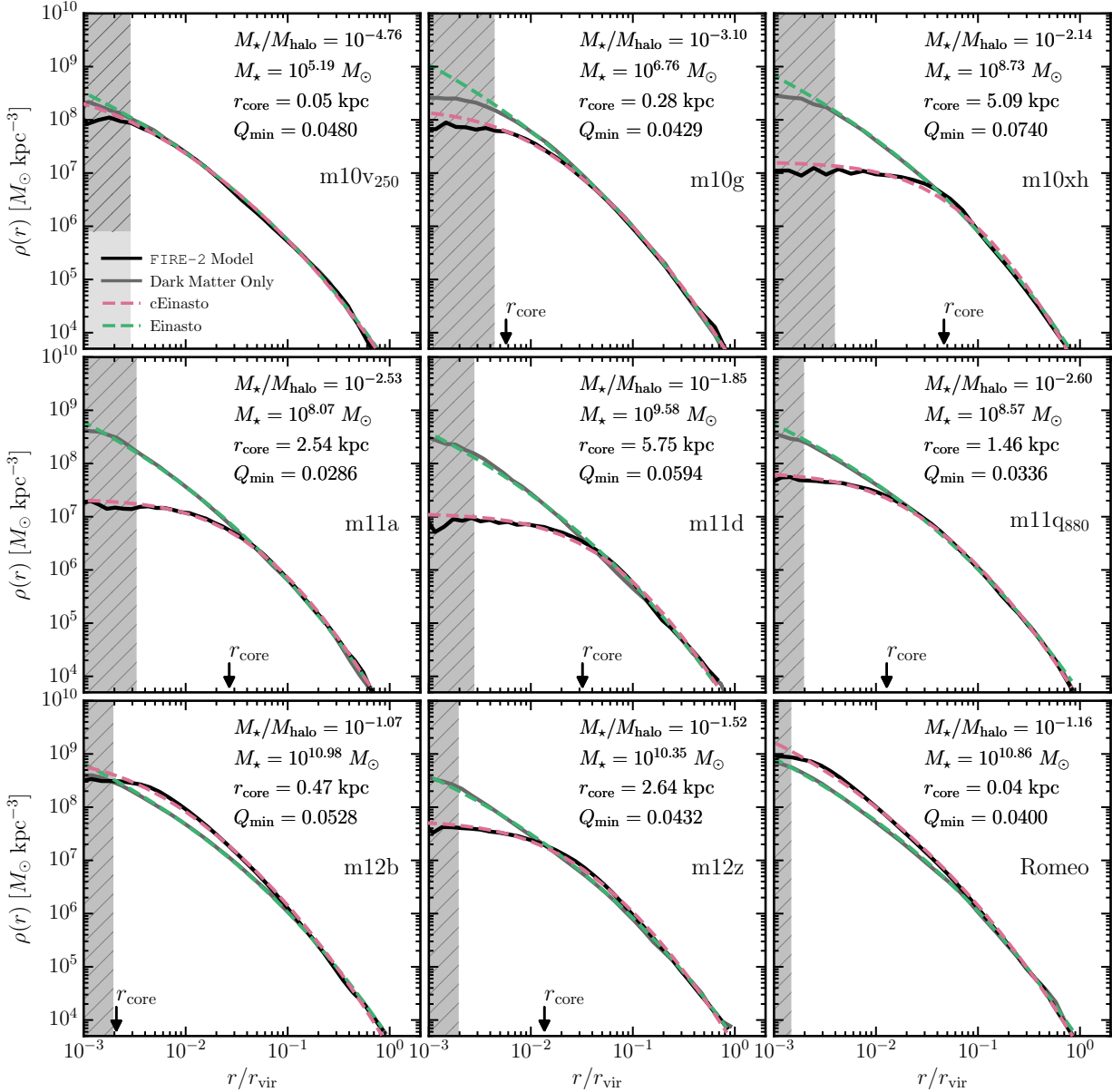


Figure 4. — *Profiles of the local dark matter density:* The ρ_{cEin} fits (pink dashed curves, with $\alpha_\epsilon = 0.16$) are plotted along with the FIRE-2 galaxies (black curves) for a sample of galaxy halos. The ρ_{Ein} fits (green dashed curves, with $\alpha_\epsilon = 0.16$) to the density profiles of DMO analogs (grey curves) are plotted as well. The vertical grey band encloses the radius where numerical two-body relaxation might effect the halo. Each panel has a list of relevant parameters for each galaxy: the stellar mass fraction (M_\star/M_{halo}), the stellar mass (M_\star), the dark matter core radius from the ρ_{cEin} profile fit (r_c), and the minimum value of the merit function (Q_{min}) that indicates the goodness-of-fit. The fitted dark matter core radius, r_c , is indicated by the black arrow pointing along the radial axis to show its location in units of r_{vir} . For most of the depicted galaxies, the ρ_{cEin} profile fits perform exceptionally well in parameterizing the location of r_c . Note that these examples include the full range of fit quality in our sample (as measured by Q_{min}), including some of the poorest fits, e.g., m10xh in the upper right corner.

four classifications of halos in our full-physics runs: “cusps”, “small cores”, “large cores”, and “Milky Way-mass halos”. The halos simulated with FIRE-2 physics are plotted as colored solid curves while their respective DMO analogs are shown as dashed lines with the same color. Starting with the upper-left panel, low-mass dwarfs tend to be hosted by cuspy dark matter halos. Similarly, halos with small cores tend to host higher-mass classical dwarfs. Halos with the largest cores correspond the brightest dwarf galaxies, which

we have seen previously in Fig 2, while MW-mass galaxies have dark matter halo profiles that are more complicated (and are discussed further below). For reference, the solid black line shows the log-slope of the Einasto profile, Eq. (3). The galaxies and DMO analogs have their radii normalized by r_{-2} from the DMO runs.

As expected, Eq. (3) captures the log-slope trend of the DMO halos. The same is true for FIRE-2 runs with low stellar mass fraction (“cusps” in this case). Halos labeled

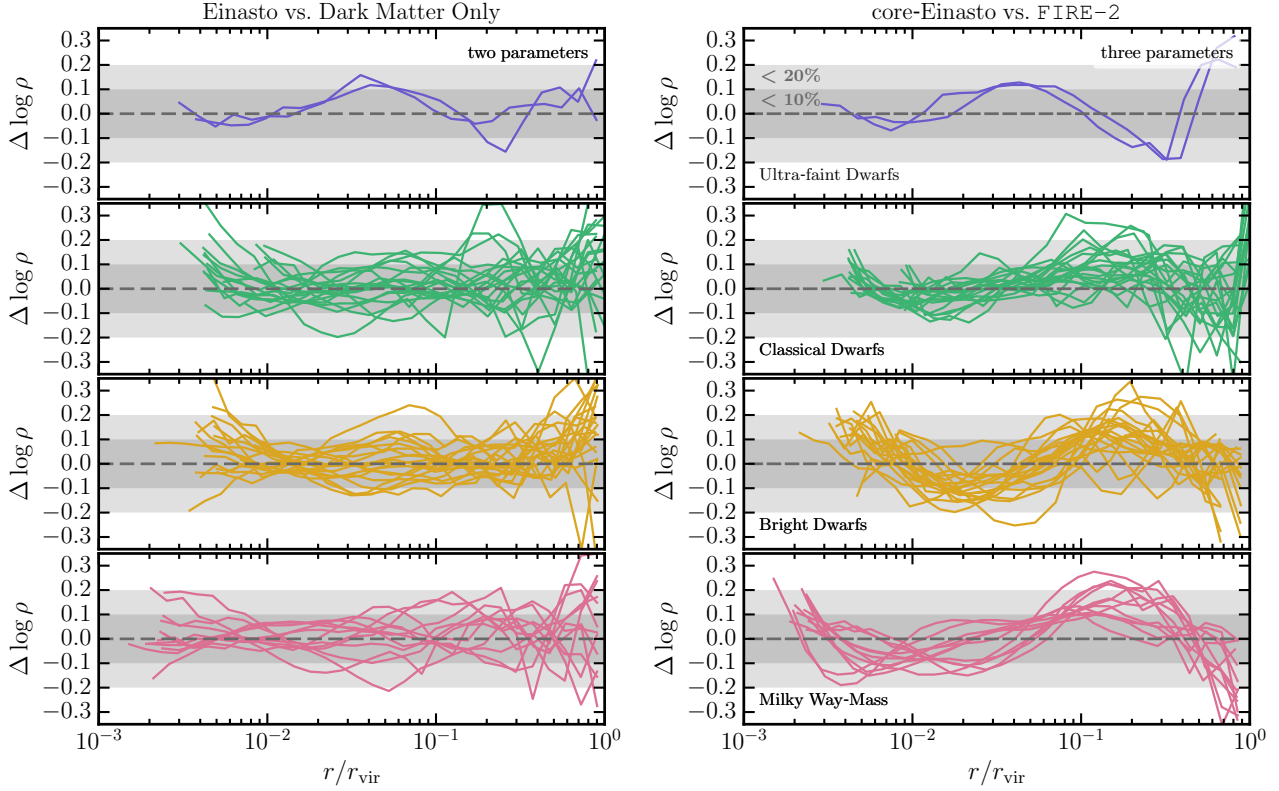


Figure 5. — *Profile residuals*: Deviation from the best profile fits for each individual halo (fit subtracted from simulation). The left column shows residuals for fits to our DMO analogs using Einasto profiles with $\alpha_\epsilon = 0.16$. The right column shows residuals for the hydrodynamic simulations of the same halos fit using the core-Einasto profile with $\alpha_\epsilon = 0.16$. For clarity, we have grouped halos by the four classification groups discussed in Section 2 in each row: ultra-faint dwarfs, classical dwarfs, bright dwarfs, and MW-mass halos. Residuals are computed from the inner-most resolved radius, r_{conv} , out the virial radius of each halo. The darker and lighter shaded gray enclose residuals of 10% and 20%, respectively. The core-Einasto fits to the full physics runs are almost as good as the Einasto fits are for the DMO halos. The offsets are less than 15% in the inner regions of classical dwarfs and most bright dwarfs. Several of MW-size halos show worse fits, with offsets as large as 20%, which is a result of both baryonic contraction and feedback-induced dark matter cores.

“small cores” tend to slightly deviate from Eq. (3), with upturns in the log-slope trend for $r \lesssim 0.03 \times r_{-2}$. The lower left panel contains galaxy halos (solid lines) that approach $d \log \rho / d \log r = 0$ at small radii – that is, a true core. This behavior never occurs beyond r_{-2} of the analogous DMO profiles, and cores are only seen at $r \ll r_{-2}$. MW-mass halos have more complicated profiles. Their log-slopes tend to lie below the log-slope of DMO analogs from $r \approx [0.1 - 1] \times r_{-2}$; this is a consequence of baryonic contraction. However, we see that at $r \ll r_{-2}$, the log-slopes begin to rise towards 0, indicating that small cores can form in our MW sample.

In order to capture the behavior illustrated in Fig. 3, we start by writing a more general form of Eq. (3) that allows the log-slope to increase more sharply within a physical core radius, r_c :

$$\frac{d \log \rho}{d \log r}(r) = -2 \left(\frac{r}{\tilde{r}_s} \right)^{\alpha_\epsilon} \tilde{C}(r|r_c). \quad (5)$$

Implemented here is a radially-dependent damping function, $\tilde{C}(r|r_c)$, which is designed to control the rate of which the profile dampens within r_c . The variable \tilde{r}_s plays a similar role as r_{-2} in Eq. (3), but will no longer be the radius where the log-slope is equal to -2 owing to the presence of r_c . We demand that the behavior of the damping function satisfies

the limiting cases of $\tilde{C} \rightarrow 1$ and $\tilde{r}_s \rightarrow r_{-2}$ as $r_c \rightarrow 0$ in order to (i) capture the qualitative expectations of cores that can substantially vary in size and (ii) revert back to the form of ρ_{Ein} in the absence of a core.

We adopt the following form:

$$\tilde{C}(r|r_c) = \left(1 + \frac{r_c}{r} \right)^{\alpha_\epsilon - 1}, \quad (6)$$

such that

$$\frac{d \log \rho}{d \log r}(r) = -2 \left(\frac{r}{\tilde{r}_s} \right)^{\alpha_\epsilon} \left(1 + \frac{r_c}{r} \right)^{\alpha_\epsilon - 1}. \quad (7)$$

In particular, the log-slope of the density profile approaches zero more quickly for larger values of r_c . Integrating out Eq. (7) gives us a cored counterpart of ρ_{Ein} , the *core-Einasto* profile:

$$\log \left[\frac{\rho_{\text{cEin}}(r)}{\tilde{\rho}_s} \right] = -\frac{2}{\alpha_\epsilon} \left[\left(\frac{r + r_c}{\tilde{r}_s} \right)^{\alpha_\epsilon} - 1 \right]. \quad (8)$$

Here, $\tilde{\rho}_s$ is a density free parameter in the fit. In what follows we set $\alpha_\epsilon = 0.16$, which reduces the expression to a three-parameter profile. In the limiting case of $r_c \rightarrow 0$, we re-acquire ρ_{Ein} , where now $\tilde{\rho}_s \rightarrow \rho_{-2}$. Note that the central density with the presence of a core, $\rho_0 := \rho_{\text{cEin}}(r = 0)$, is

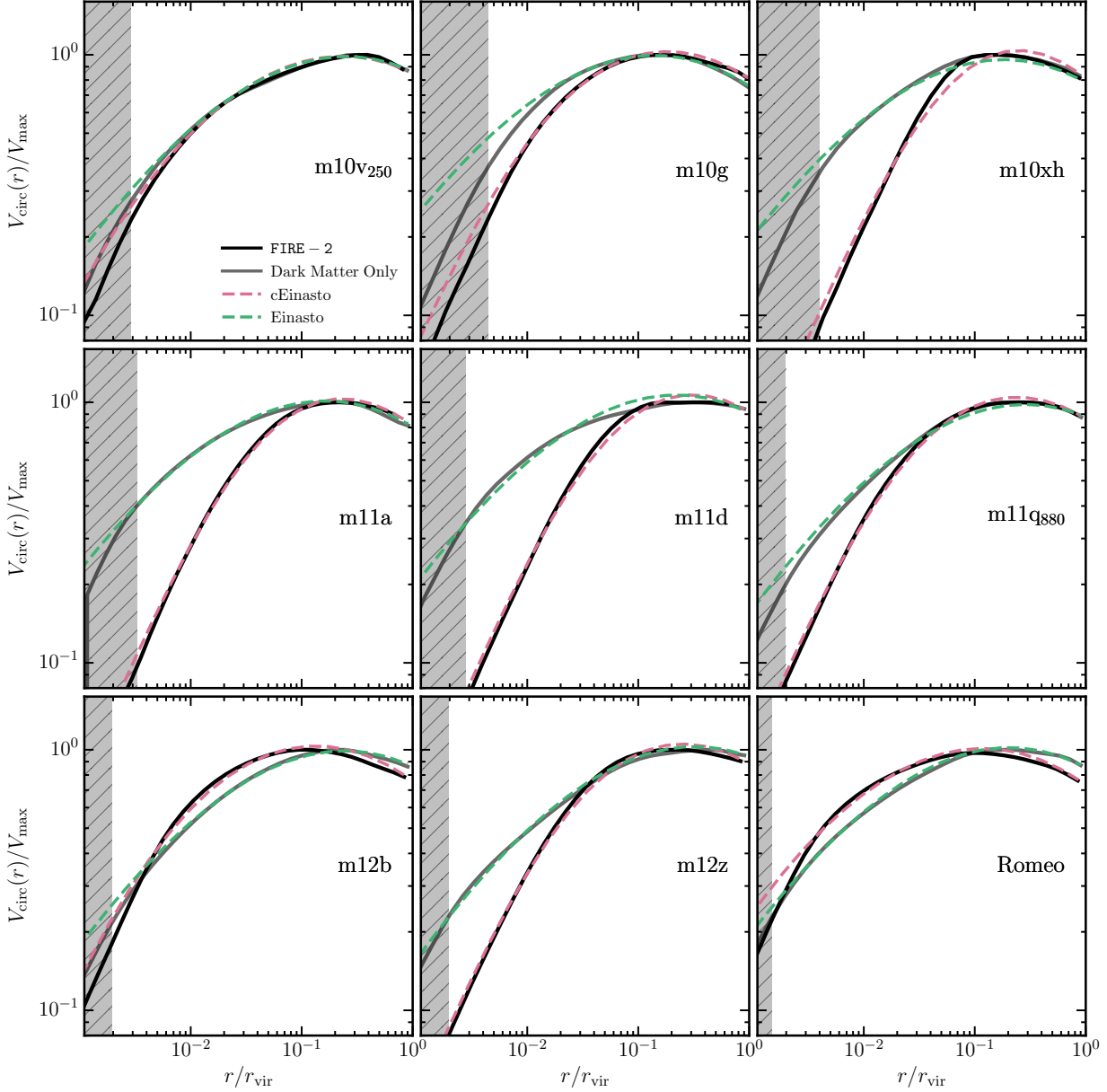


Figure 6. — *Dark matter circular velocity curves.* Shown are the dark matter components of the circular velocity curves, $V_{\text{circ}}(r) = \sqrt{GM(<r)/r}$, of the same halos presented in Fig. 4. The dashed pink and green curves are plotted using the analytical forms of Eqs. (B5) and (B6), respectively. Curves of V_{cEin} and V_{Ein} are normalized by V_{max} of the galaxy and DMO analog, respectively. Analytical fits are able to capture the density normalization of the simulated halos robustly for all of the dwarf galaxies, even while it can under-estimate or over-estimate the integrated mass in at the outer radii.

parametrized as

$$\rho_0 = \tilde{\rho}_s \exp \left\{ -\frac{2}{\alpha_\epsilon} \left[\left(\frac{r_c}{\tilde{r}_s} \right)^{\alpha_\epsilon} - 1 \right] \right\}. \quad (9)$$

Alternatively, we can reparameterize $\tilde{\rho}_s$ by mapping to $\tilde{\rho}_{-2} := \rho_{\text{cEin}}(r_{-2})$, the density (and radius) where the log-slope is equal to -2 . This allows us to re-express Eq. (8) as

$$\log \left[\frac{\rho_{\text{cEin}}(r)}{\tilde{\rho}_{-2}} \right] = -\frac{2}{\alpha_\epsilon} \left[\left(\frac{r+r_c}{\tilde{r}_s} \right)^{\alpha_\epsilon} - \left(\frac{r_{-2}+r_c}{\tilde{r}_s} \right)^{\alpha_\epsilon} \right], \quad (10)$$

which certainly work in our zero core limit to re-acquire Eq. (4). However, this expression now introduces an addi-

tional free parameter, r_{-2} , that can likely lead to degenerate results in acquiring r_c and \tilde{r}_s . With that, we prefer to adopt the form of Eq. (8) for our analysis hereinafter. Analytic expressions for the mass profile, gravitational potential, and energy for the core-Einasto profile are presented in Appendix B.

4.3 Resulting profile fits

All functional fits are performed using the Levenberg-Marquart minimization algorithm. We restrict our radial density profile fits to the radial range of r_{conv} to r_{vir} . Best-fit

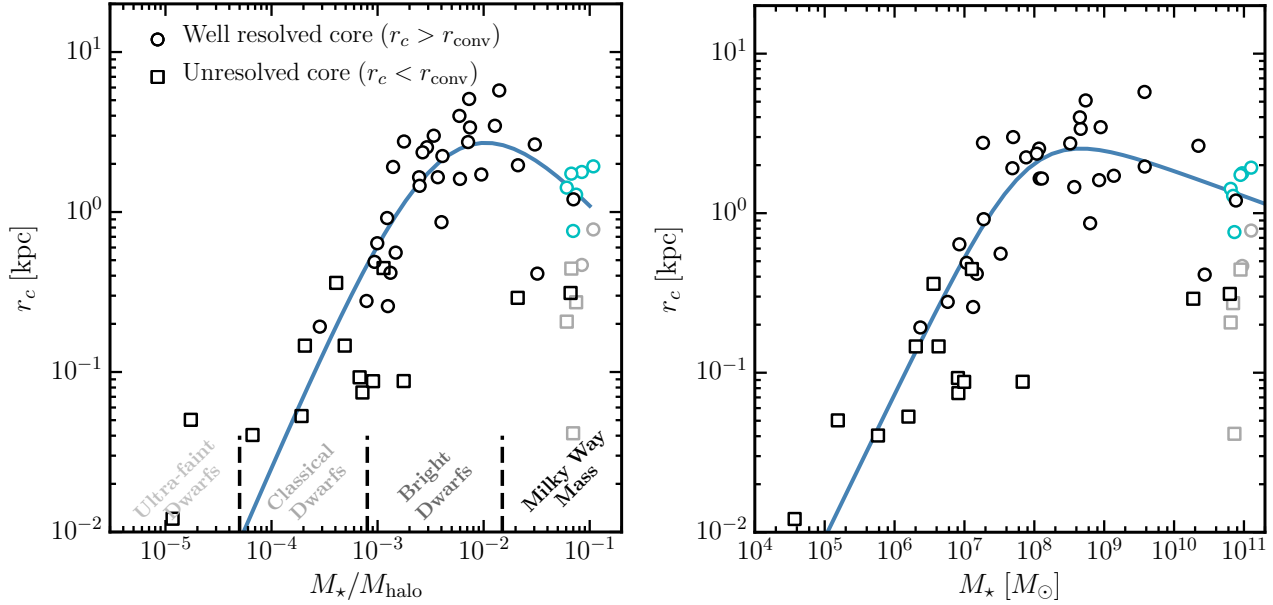


Figure 7. — *Feedback-induced core formation.* Circles show core radii that are larger than the convergence radius of the simulation ($r_c > r_{\text{conv}}$) while squares are values smaller than the convergence radius ($r_c < r_{\text{conv}}$). MW halos with significant baryonic contraction, which are therefore not as well fit by the ρ_{cEin} function, are shown in light grey. The cyan points show r_c values for MW-mass galaxies returned from a four-parameter “baryonic contracted cored-Einasto” profile, $\rho_{\text{cEin,BC}}$, introduced in Appendix C, in order to better account for baryonic contraction. **Left:** Core radius as a function of stellar to halo mass ratio. The solid blue curve is a fit to the dark black and cyan points using Eq. (12), with the best fit parameters given in Table 1. We note that this trend mirrors results shown in Fig. 1, with the largest core radii values occurring in the “Bright Dwarfs” regime. **Right:** Dark matter core radius as a function of M_* . Peak core formation, while scattered, appears around $M_* = 10^{8-9} M_\odot$. The solid blue curve is our best fitting line using Eq. (12) and best-fit parameters from Table 1 for $x = M_*$.

models are obtained by simultaneously adjusting the parameters of the analytical density profiles in order to minimize a figure-of-merit function, defined by

$$Q^2 = \frac{1}{N_{\text{bins}}} \sum_i^{N_{\text{bins}}} \left[\log_{10} \rho_i - \log_{10} \rho_i^{\text{model}} \right]^2, \quad (11)$$

which weights all the logarithmic radial bins equally and, for a given radial range, is fairly independent of the number of bins used (Navarro et al. 2010). That is, the minimum figure-of-merit, denoted as Q_{min} , quantifies the residuals of the true profile from the model caused by shape differences induced in the fitting routine.

4.3.1 Local dark matter density

Fig. 4 provides example fits for a sample of dark matter density profiles. Dark matter halos simulated using FIRE-2 (black curves) are fitted with ρ_{cEin} (pink dashed) while the DMO analogs (grey line) are fitted with ρ_{Ein} (dashed green). In each panel, we list the galaxy’s stellar mass fraction (M_*/M_{halo}), stellar mass (M_*), dark matter core radius (r_c) given by fitting ρ_{cEin} , and the goodness-of-fit (Q_{min}) from fitting ρ_{cEin} . The location of the best-fit dark matter core radius, scaled by the virial radius, is indicated by the black arrow in each panel. Table E2 lists the fit results for all of our galaxies, including the fit parameters and the Q_{min} values. We can see that the value r_c is effectively determined for a wide range of galaxy sizes. For even the worst profile fits (e.g. m10xh with $Q_{\text{min}} = 0.074$; top-right panel), the value

of r_c is still identified at the location where one’s eye might pick out a dark matter core in the local density profile.

As a way of examining the robustness of Eq. (8), we fit core-Einasto to the DMO analogs and found that in every case the best-fit core-radii were either zero or smaller than the radius of convergence. This provides confidence that this profile does not force or impose cores that do not exist in the resolved regions of the halo. However, it does suggest that r_c values smaller than the convergence limit should not be taken as robust indications for the existence of real cores. For example, the upper left panel of Fig. 4 shows an ρ_{cEin} fit to m10v₂₅₀ (baryon simulated), a profile that is unaltered by feedback in the resolved region owing to its small stellar mass. The best-fit core radius ($r_c \approx 50$ pc) is much smaller than the radius of convergence ($r_{\text{conv}} \approx 160$ pc) in this case.

While we find success in characterizing dwarf galaxies with ρ_{cEin} , almost all of the MW-mass halos have cored regions that are more sharply pronounced than enabled by the ρ_{cEin} profile. As one can see (e.g. m12b and Romeo), the values of r_c from the fits do not coincide with the locations of the bend seen in the simulated profiles.⁷ Based on our entire sample of MW-mass halos, we find that the ρ_{cEin} profile performs less well for MW-mass halos that have both a small central dark matter core and baryonic contraction in the inner densities. On the other hand, MW-mass halos with

⁷ The core radius of Romeo from the ρ_{cEin} fit does not appear in Fig. 4 (bottom right panel) since the fitted value of r_c is located inside the region of numerical convergence ($r_c/r_{\text{vir}} < 10^{-3}$).

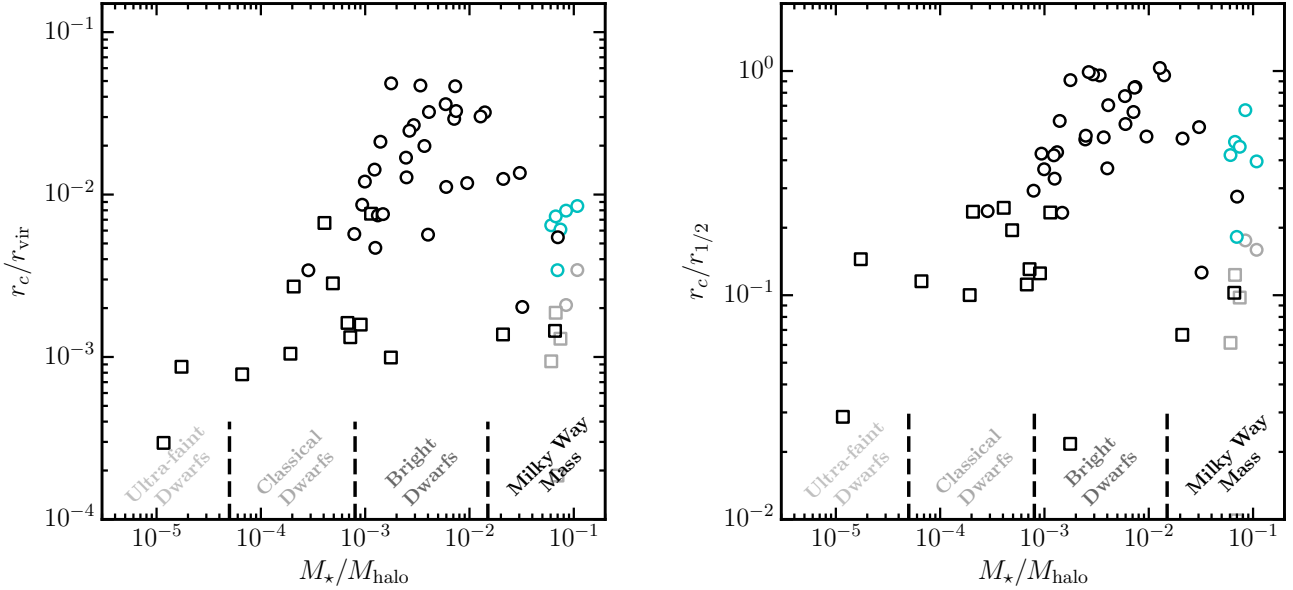


Figure 8. — *Core radius relative to the halo and galaxy size.* Similar to Fig. 7, except with the core radii scaled by the virial radius of the dark matter halos (left) and stellar-half-mass radius of the galaxies (right). **Left:** The fractional size of cores rises toward the regime of peak core formation, where $r_c \approx 0.05 r_{\text{vir}}$. MW-mass halos have r_c/r_{vir} values comparable to those of dwarf galaxies with $M_{\star}/M_{\text{halo}} \sim 10^{-3}$. **Right:** All resolved cores are constrained to a lower bound of $r_c \gtrsim 0.1 r_{1/2}$. At peak core formation, $r_c \approx r_{1/2}$ for some of the the brightest dwarfs.

little evidence of either baryonic contraction (e.g. m12z) or a core are successfully characterized by ρ_{cEin} . MW-mass halos with no core, but with only baryonic contraction, are also well-modeled by ρ_{Ein} . In Appendix C, we formulate a more general core profile with one additional free parameter that captures the behavior for baryonic contracted halos with cores. This allows us to accurately quantify the core radii for the rest of our MW-mass halos.

4.3.2 Density profile residuals

Profile residuals of the local dark matter density are presented in Fig. 5 for DMO analog fitted with the Einasto profile (left) and to the dark matter halos of the FIRE-2 physics runs fit to core-Einasto (right). Results are split into the four galaxy classifications defined in Section 2. The residuals for the left and right columns are comparable, which is remarkable given that the right-hand fits have only one additional free parameter to account for the full impact of complex galaxy formation physics. Notice that the largest deviations are present large radii ($r \gtrsim 0.3 r_{\text{vir}}$). This behavior has been seen in the past for DMO halos, where the outer regions may not be fully relaxed (e.g. Ludlow et al. 2010, 2016), and may contain large substructures.

While we have only two ultra-faint galaxies (blue curves) in our sample, both galaxies are well described to 10% for a majority of the radii. This is unsurprising, as these halos lack the requisite star formation to induce cores; the core-Einasto fit is therefore effectively the same as a standard Einasto fit, with r_c values that are smaller than the convergence radius. Almost all of the classical dwarf galaxies (green curves) have excellent core-Einasto fits, with deviations in the range 10 – 15% at worst. At small radii

($r \lesssim 0.1 \times r_{\text{vir}}$), core-Einasto is shown to be sufficient in fitting the FIRE-2 halos compared to their DMO analogs in the same radial regions. For a majority of the brightest dwarfs in our sample, deviations are constrained within 15%. For MW-mass halos, the quality of the fit can range from quite good to as bad as 20%. As mentioned previously, the worst fits are for the MW-mass halos impacted by both baryonic contraction and feedback-induced core formation at small radii. We find deviations of 10 – 15% in the inner-most regions for profiles of MWs with just cores (e.g. m12z in Fig. 4) or just having baryonic contraction with no cores.

In both columns, there are hints of a sinusoidal feature in the residuals. This behavior is not unusual when simplified fits are compared to detailed dark matter halo profiles (e.g. Griffen et al. 2016). Reducing the residual behavior even more would require more free parameters in the form of \bar{C} in Eq. (5) and/or allowing the value of α_{ϵ} to vary from halo-to-halo. However, given that the gross residuals for our core-Einasto fits to the FIRE-2 runs are close to those of Einasto fits to DMO runs, we are satisfied that the given parameterization provides a useful balance between simplicity and accuracy. In Appendix D we do find that our halos are modeled better by the three-parameter core-Einasto profile than two alternative three-parameter profiles: the core extension for the NFW from Peñarrubia et al. (2012) and Dekel+ from Dekel et al. (2017) and Freundlich et al. (2020).

4.3.3 Dark matter circular velocity

Fig. 6 provides an alternative view of the results shown in Fig. 4: it shows the circular velocity curves of the dark mat-

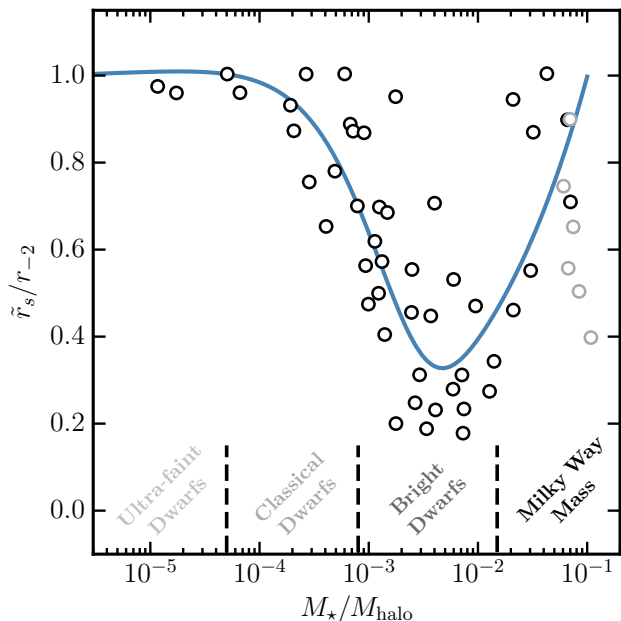


Figure 9. — *Effects of core formation on the global structure of the dark matter halo.* A trend can be seen between the fitting parameter, \tilde{r}_s , and the interpolated scale radius, r_{-2} , from the ρ_{cEin} profile. We again show the results not well fitted with ρ_{cEin} , which are highlighted in light grey like in Fig 7. As the core radius of the halos becomes larger, i.e. as we increase $M_\star/M_{\text{halo}} \sim 5 \times 10^{-3}$, the physical interpretation of \tilde{r}_s changes. This result shows that the formation of a core (found most prominently in the regime of the bright dwarfs) results in a change to the dark matter halo at larger scales (as parametrized by r_{-2}). The solid blue curve is our best fits using Eq. (13).

ter component,⁸ $V_{\text{circ}}(r) = \sqrt{GM(<r)}/r$, for the same halos presented in Fig. 4, each normalized by $V_{\text{max}} := \max[V_{\text{circ}}(r)]$ of the dark matter curve. The analytical profiles for V_{cEin} and V_{Ein} are plotted using Eqs. (B5) and (B6), respectively, for the values obtained from the fits shown in Fig. 4. These analytical curves are normalized by the V_{max} values of the simulated halos to which they are fitted. For profile fits over-estimating (or under-estimating) the mass found in the simulated profiles by 15 – 20% (e.g., m10xh and m11d), the most substantial effects can be seen at the outer radii, near where V_{max} is attained. However, even for the worst profile fits in our sample, *the central density normalization is well-captured for dwarf galaxies of varying stellar mass fractions.*

4.4 Parametrization of the physical core radius

For the left plot in Fig. 7, we show the relationship between M_\star/M_{halo} and the fitted values of r_c . Circular points denote the values of r_c that we verify as resolved cores (with $r_c > r_{\text{conv}}$ for the local dark matter density profiles). This sample includes the MW-mass core radii fit using using the

⁸ For the analysis of observed galaxies, spherically averaged rotation curves are typically presented using their total mass, i.e., their combined baryonic and dark matter components. We chose to show just the dark matter components here to compare with our core-Einasto model.

Table 1. Best-fit parameters for the physical core radius, r_{core} . For complete data set: $-3.54 \lesssim \log_{10}(M_\star/M_{\text{halo}}) \lesssim -0.97$ and $6.37 \lesssim \log_{10}(M_\star/M_\odot) \lesssim 11.10$.

Parameter	\mathcal{A}_1	\mathcal{A}_2	x_1^*	x_2^*	β_1	γ_1
M_\star/M_{halo}	1.21	0.71	7.2×10^{-3}	0.011	2.31	1.55
M_\star/M_\odot	1.33	4.3×10^7	1.93	0.55	1.06	0.90

Note. Use Eq. (12) for either $x = M_\star/M_{\text{halo}}$ or $x = M_\star/M_\odot$.

four parameter function $\rho_{\text{cEin,BC}}$ (cyan highlights) described in Appendix C instead of their r_c values from ρ_{cEin} (shown by gray points for reference). Squares denote best-fit core radii that have values smaller than the numerical convergence region ($r_c < r_{\text{conv}}$). It is important to note that in some cases, we obtain fit values of r_c that are formally smaller than r_{conv} yet large enough that the halo is not well-described by the standard ρ_{Ein} form. This comes about because dark matter halos impacted by stellar feedback produce dark matter profiles that are no longer self-similar in nature, meaning the core-Einasto fit balances \tilde{r}_s and r_c to accommodate the shape of the density profile.

We see that our robustly-determined r_c values ($r_c > r_{\text{conv}}$), begin to appear at the higher mass end for the classical dwarf galaxy regime, $M_\star/M_{\text{halo}} \gtrsim 7 \times 10^{-3}$, with values that are physically quite small, $r_c \approx [0.2 - 0.3]$ kpc. As the stellar mass fraction increases toward the region of bright dwarf galaxies, $M_\star/M_{\text{halo}} \approx [10^{-3} - 10^{-2}]$, the sizes of the core radii, r_c , increase with M_\star/M_{halo} . Importantly, the largest dark matter cores, $r_c \approx [5 - 6]$ kpc, coincide with the stellar mass fraction at the peak core formation that we have seen previously ($M_\star/M_{\text{halo}} \approx 5 \times 10^{-3}$). A majority of the galaxies at the MW-mass scale have dark matter cores as $r_c \approx 1 - 2$ kpc, though two remain fairly cuspy (m12r and m12w). To provide further insight into observations of real galaxies comparable to the simulations analyzed here, the right plot in Fig. 7 shows the trend of r_c with M_\star . The largest cores tend to form in galaxies with $M_\star \approx 10^{8-9} M_\odot$. Notably, a significant amount of scatter is seen for fixed value of $r_c \approx 2 - 3$ kpc, which tends to be apparent for galaxies with $M_\star \approx 10^{8-11} M_\odot$.

The formation of small cores for MW-mass halos using FIRE-1 was discussed in Chan et al. (2015), where they found that small cores for MW-size galaxies tend form in the low-mass galaxy progenitors at $z \sim 2$, which have stellar-to-halo mass ratios suitable for core formation. These progenitors have their resulting innermost dark matter profile amplified at $z = 0$ due to baryonic contraction. This phenomena also drives out old stars formed in situ in MW-like galaxies (El-Badry et al. 2018b). Other simulation groups have not reported the existence of small cores at the MW-mass regime. This could however be due to differences in numerical resolution. For example, the NIHAO simulations presented in Tollet et al. (2016) and Macciò et al. (2020) study MW-mass halos at a lower resolution than ours, with convergence down to $r_{\text{conv}} \approx 1.25$ kpc compared 330-500 pc in our runs (see Table E1). The MW cores in our simulations are ~ 1 kpc in size. Such cores would be difficult to form without having a convergence radius smaller than this limit.

We find that the relationship between r_c and $x =$

Table 2. Best-fit parameters for \tilde{r}_s/r_{-2} .

Parameter	\mathcal{B}	x_3^*	x_4^*	β_2	γ_2
M_\star/M_{halo}	1.51	0.044	0.28	31.79	0.40
M_\star/M_\odot	0.098	5.1×10^6	1.4×10^6	0.57	0.20

Note. Use Eq. (13) for either $x = M_\star/M_{\text{halo}}$ or $x = M_\star/M_\odot$.

M_\star/M_{halo} (and $x = M_\star/M_\odot$) can be captured as a double-power law

$$r_c(x) = 10^{\mathcal{A}_1} \left(\mathcal{A}_2 + \frac{x}{x_1^*} \right)^{-\beta_1} \left(\frac{x}{x_2^*} \right)^{\gamma_1} \text{ kpc}, \quad (12)$$

where $\{\beta_1, \gamma_1\}$ are free parameter slopes that control the transition of x . The quantities $\{x_1^*, x_2^*\}$ are normalization parameters associated with both slopes, and $\{\mathcal{A}_1, \mathcal{A}_2\}$ are constants of the fit. Best-fit parameters for $x = M_\star/M_{\text{halo}}$ and M_\star/M_\odot are given in Table 1. The trend for our plotted data for r_c as a function of M_\star/M_{halo} and M_\star/M_\odot is shown by the blue curves in the left and right plots in Fig. 7, respectively.

Fig. 8 is similar to left plot in Fig. 7 except with the values of r_c normalized by the size of the dark matter halo virial radius (r_{vir} ; left plot) or the half-stellar-mass radius of the galaxy it hosts ($r_{1/2}$; right plot) as a function of M_\star/M_{halo} . Notably, the normalization for each plot roughly follows the same trend that we have seen in previous figures: as M_\star/M_{halo} increases from 10^{-4} to 10^{-2} , galaxies have larger cores, *even relative to the size of the dark matter halo or its central galaxy*. The trend peaks at the mass scale of robust core formation. At this peak, the brightest galaxies tend have cores of $r_c \sim 0.04 r_{\text{vir}}$ (albeit with large scatter) and $r_c \sim r_{1/2}$. Interestingly, most MW-mass halos have r_c/r_{vir} values similar to dwarfs with stellar fractions that are 100 times lower and $r_c/r_{1/2}$ values comparable to many of the brightest dwarfs.

4.5 Parametrization of \tilde{r}_s

We wish to quantify how the free parameter, \tilde{r}_s , is related to r_{-2} from using ρ_{cEin} , the radius at which the log-slope of the local dark matter density is equal to -2 , in the presence of a dark matter core. Unfortunately, the relation between \tilde{r}_s and r_{-2} for the FIRE-2 dark matter halos cannot be solved analytically as the additional power of α_ϵ means they are non-linearly related. However, we can parametrize the covariance between \tilde{r}_s and r_{-2} from introducing r_c . Fig. 9 shows the ratio of \tilde{r}_s to r_{-2} as a function of M_\star/M_{halo} for the FIRE-2 halos. Here, r_{-2} is interpolated from only the ρ_{cEin} fits. As expected, dwarf galaxies with no cores (or cores small enough to effectively be approximated as $r_c = 0$) have $\tilde{r}_s \simeq r_{-2}$. As we transition towards the region of peak core formation, \tilde{r}_s gradually decreases relative to r_{-2} . We then see a sudden upturn at the MW-mass scale, which is a consequence of baryonic contraction. The relation for \tilde{r}_s to r_{-2} as a function of M_\star is also discussed in Appendix A.

The relationship between \tilde{r}_s/r_{-2} and either $x = M_\star/M_{\text{halo}}$ (or $x = M_\star/M_\odot$) can be captured as a double-

power law:

$$[\tilde{r}_s/r_{-2}](x) = \left(1 + \frac{x}{x_3^*} \right)^{-\beta_2} + \mathcal{B} \left(\frac{x}{x_4^*} \right)^{\gamma_2}, \quad (13)$$

where $\{\beta_2, \gamma_2\}$ are free parameter slopes that control the transition, the quantities $\{x_3^*, x_4^*\}$ are normalization values associated with these slopes, and \mathcal{B} is a constant. The best fit parameters for $x = M_\star/M_{\text{halo}}$ are given in Table 2. The trend for our data is plotted as the blue curve in Fig. 9.

4.6 Parametrization of the halo concentration

The stellar feedback in dark matter halos also affects the halo concentration through the gravitational coupling of dark matter to the rapidly changing central gravitational potential. We adopt the halo concentration parameter $c_{\text{vir}} := r_{\text{vir}}/r_{-2}$. This definition of c_{vir} will be applied for the established results modeled by ρ_{cEin} , $\rho_{\text{cEin,BC}}$, and ρ_{Ein} .⁹ Ratios of the concentration parameter between the FIRE-2 halos, c_{F2} , and their DMO analogs, c_{DM} , are shown in the left panel of Fig. 10 as a function of M_\star/M_{halo} . The result from Di Cintio et al. (2014b) is plotted as the pink curve. We also extend this discussion with the parametrization done for M_\star in Appendix A.

Galaxies with lower stellar mass fraction limit ($M_\star/M_{\text{halo}} \lesssim 10^{-4}$) have values of c_{vir} comparable to their DMO analogs. Noticeable differences of the concentrations become apparent as M_\star/M_{halo} starts to increase towards the classical dwarf and bright galaxy regime. Importantly, as M_\star/M_{halo} approaches the peak of sufficient core formation, the halo concentrations for the FIRE-2 galaxies are conspicuously smaller – by 30-50% – than the halo concentrations of their DMO analogs. This could mean that the strength of stellar feedback, which we can also probe by the size r_c , in these halos has been strong enough to affect the density structure out to r_{-2} , an effect not seen previously (e.g., compare with the pink curve from Di Cintio et al. (2014b)). However, the relation from Di Cintio et al. (2014b) used the parameters obtained from fitting the $\alpha\beta\gamma$ -profile to acquire r_{-2} while we numerically interpolated from our resulting profile fits. We explore the differences in concentration that arise for the same halos when fitting different profiles in Appendix D. We find that when using the $\alpha\beta\gamma$ -profile, the concentration can shift somewhat, but there is a tendency to be lower in the bright dwarf regime, following a similar qualitative trend shown in Fig. 10.

As stellar fractions reach the the MW regime, we see the opposite effect: the concentrations of our galaxy halos are significantly larger than their DMO analogs because of baryonic contraction.

The relationship between the concentration parameters of our galaxy halos can be parameterized as a double power law:

$$[c_{\text{F2}}/c_{\text{DM}}](x) = \left(1 + \frac{x}{x_5^*} \right)^{-\beta_3} + C \left(\frac{x}{x_5^*} \right)^{\gamma_3}, \quad (14)$$

⁹ For the FIRE-2 halos fitted well with ρ_{cEin} and the MWs fitted with $\rho_{\text{cEin,BC}}$ in Appendix C, the value of r_{-2} is interpolated from the analytical profile fits, while for the DMO halos, r_{-2} is taken from the free parameter fit of ρ_{Ein} .

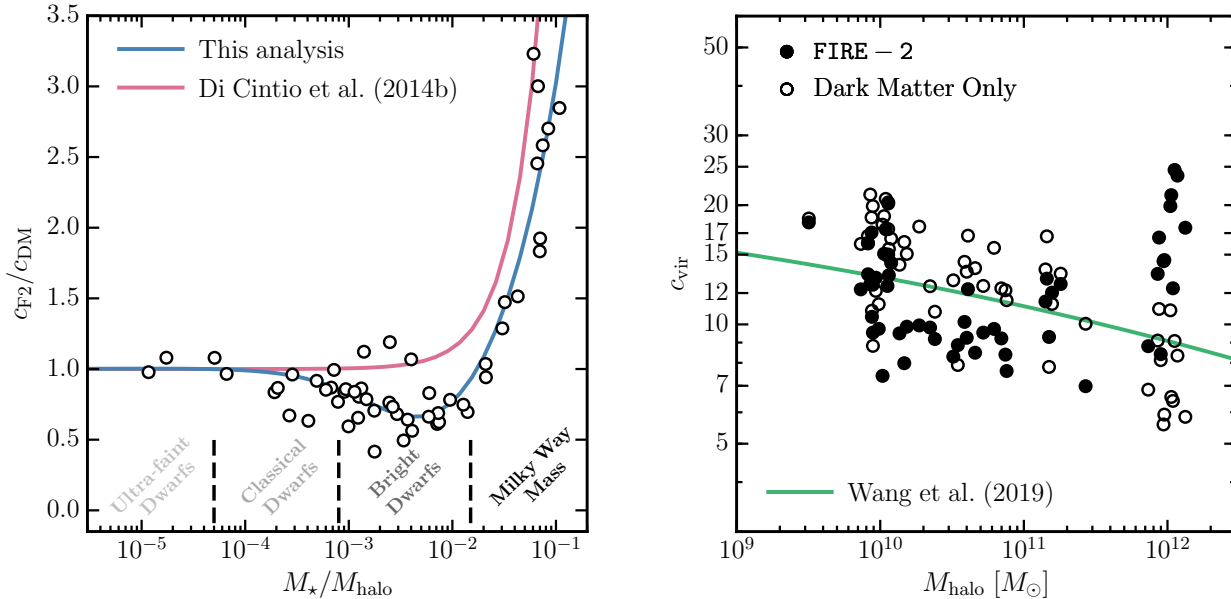


Figure 10. — *The impact of feedback on halo concentration.* Halo concentration defined by $c_{vir} := r_{vir}/r_{-2}$. **Left:** FIRE-2 halo concentrations (c_{F2}) using r_{-2} interpolated from the best fits of ρ_{cEin} and best fits of $\rho_{cEin,BC}$ from Appendix C. For the halo concentrations of the DMO analogs (c_{DM}), r_{-2} is taken from the free parameter fit of ρ_{Ein} . Galaxies with have the largest cores (the brightest dwarfs) have their halo concentrations lowered by a factor of two compared to DMO analog concentrations. The solid blue curve is our best fit of the scatter points using Eq. (14). Also plotted is the fit from Di Cintio et al. (2014b) as the solid pink curve for comparison. **Right:** Concentration as a function of dark matter halo mass. Galaxies and DMO analogs are denoted by the filled and unfilled black circles, respectively. The solid green curve is the concentration relation from Wang et al. (2019), which was also calibrated using the c_{vir} from the Einasto profile (including the same shape considered here, $\alpha_\epsilon = 0.16$).

Table 3. Best-fit parameters for c_{F2}/c_{DM} .

Parameter	C	x_5^*	β_3	γ_3
M_*/M_{halo}	0.374	4.28×10^{-3}	1.80	0.66
M_*/M_\odot	6.39×10^{-4}	1.77×10^5	0.057	0.62

Note. Use Eq. (14) for either $x = M_*/M_{halo}$ or $x = M_*/M_\odot$.

where either $x = M_*/M_{halo}$ or $x = M_*/M_\odot$, $\{\beta_3, \gamma_3\}$ are slopes, and x_5^* is a free normalization value to anchor the transition between slopes, and C is a constant. Best fit parameters for $x = M_*/M_{halo}$ are given in Table 3. The trend for our data is plotted as the blue curve in the left plot of Fig. 10.

The right plot in Fig. 10 shows the dark matter halo concentration directly: c_{vir} as a function of the dark matter halo mass, M_{halo} . Black filled circles are the results for the FIRE-2 halos while open circles are the DMO analogs. The solid green curve traces the recent results of the concentration-mass relation from Wang et al. (2019), which extends to masses all way down to the Earth mass dark matter halos. Note that Wang et al. (2019) uses the same concentration definition as we do as well. Additionally, they also fit halos with an Einasto profile same shape parameter we adopted ($\alpha_\epsilon = 0.16$). The DMO analogs in our halo mass range follow the Wang et al. (2019) relation with significant scatter about the median. Interestingly, galaxy halos with $M_{halo} = 10^{10-11} M_\odot$ all have about the same concentrations of $c_{vir} \approx 9$, with small scatter. In the $M_{halo} = 10^{12} M_\odot$ region, baryonic contraction of the galaxy can increase the halo

concentration significantly, to $c_{vir} \approx 15 - 25$). Observational measurements of the MW’s halo concentration, which usually assume an NFW profile, have often found values typical of those we find here for our FIRE-2 halos ($c_{vir} \approx 15 - 25$) – well above the expectation for DMO halos of that mass ($c_{vir} \sim 9$) (Battaglia et al. 2005; Catena & Ullio 2010; Deason et al. 2012; Nesti & Salucci 2013). This then also suggests that for real galaxies, the predictions from Wang et al. (2019) will be an underestimated.

5 SUMMARY AND CONCLUDING REMARKS

In this paper, we studied and modeled the $z = 0$ dark matter density profiles of 54 zoom-in galaxy simulations run using the FIRE-2 feedback model. Our sample includes galaxies with stellar masses ranging from ultra-faint dwarfs to MW-mass galaxies, a factor of around 7 decades in stellar mass and 3 decades in halo mass. Details on these simulated halos, as well as parameter fits for each dark matter halo, are provided in Appendix E.

The most significant contribution of this paper has been the introduction of the “core-Einasto”: a new, three-parameter analytic density profile that provides a good fit to our FIRE-2 galaxy halos by allowing for a prominent constant density core, Eq. (8). Specifically, our main conclusions are as follows:

- (i) We find that feedback creates prominent cores in the centers of dark matter halos that have galaxy stellar masses $M_*/M_{halo} \approx 5 \times 10^{-3}$ or $M_* \sim 10^9 M_\odot$, roughly compar-

ble to the stellar masses spanning the mass ranges of the SMC and the LMC (Fig. 2, 6, and 7). This mass regime is in agreement with previous studies (e.g. Di Cintio et al. 2014a; Tollet et al. 2016). Feedback-induced core formation becomes less important for galaxies with larger and smaller stellar masses.

(ii) We find no evidence that feedback alters the density structure of halos that host galaxies smaller than $M_\star \approx 10^6 M_\odot$ or $M_\star/M_{\text{halo}} \lesssim 10^{-4}$ down to radii $\sim 0.5\% r_{\text{vir}}$ (~ 100 pc; see also Fitts et al. 2017). This in turn results in concentration values matching those seen in DMO analogs (Fig. 10). However, in FIRE-2 simulations with higher resolution, feedback may produce cores ~ 100 pc in such galaxies (see Wheeler et al. 2019).

(iii) The core-Einasto profile, Eq. (8), takes the Einasto profile, Eq. (4), and adds one additional parameter, a core radius r_c . The profile returns to the standard Einasto form as $r_c \rightarrow 0$. With a fixed $\alpha_\epsilon = 0.16$, we find that the three-parameter core-Einasto profile is able to characterize the majority of our feedback-impacted dark matter halos almost as well as the standard two-parameter Einasto profile does for DMO halos (Figs. 4–5). In Appendix D we compare fits using the core-Einasto profile to two other three-parameter profiles (core-NFW and Dekel+) and show that the core-Einasto provides a better fit to FIRE-2 halos.

(iv) Fitted core radii are the largest ($r_c \approx 1 - 5$ kpc) for bright dwarf galaxies of $M_\star/M_{\text{halo}} \approx 5 \times 10^{-3}$ (or $M_\star \sim 10^9 M_\odot$; Figs. 7–7). Fitted core radii become smaller as the stellar to halo mass ratio moves away from this value (or equivalently, at both higher and lower stellar masses). The physical core radius is found to never be much larger than the stellar half-light radius, $r_c \lesssim r_{1/2}$, and only approaches $r_{1/2}$ in galaxies of the characteristic mass for core formation, $M_\star \sim 10^9 M_\odot$ (Fig. 8).

(v) Feedback and galaxy formation alters the global structure of dark matter halos well beyond the core region (Figs. 9–10). Halos that host bright dwarf galaxies are often less concentrated than their DMO analogs, with c_{vir} values 30% smaller. This differs slightly from the results in Di Cintio et al. (2014b), who found no change in concentration at this mass scale. At higher masses, approaching the MW scale, the trend reverses and halos become much more concentrated owing to baryonic contraction.

(vi) While baryonic contraction makes halos more concentrated and denser at the stellar half-light radius for MW size galaxies, we find that feedback can still produce small dark matter cores of $\sim 0.5 - 2$ kpc in size at this mass scale. The formation of cores in MW-size halos was previously discussed in Chan et al. (2015). The combination of core-formation and baryonic contraction makes the resultant profiles complicated enough that Eq. (8) does less well at capturing the full shape (with $\approx 20\%$ residuals, Fig. 5). To accommodate these features, we introduce a four-parameter contracted core profile in Appendix C (see Fig. C1). The presence of dark matter cores in MW-size galaxies might be supported by dynamical modeling of MW data. Portail et al. (2017) find evidence for a dark matter core comparable in size to what we quantify our feedback-affected MW-mass halos.

Though our results for core-Einasto and r_c relations have focused on halos at $z = 0$, the evolution of r_c through-

out cosmic time would provide an interesting future avenue of study, one that could provide further insight on the energy budget needed to transform cusps to cores in Λ CDM throughout cosmic time. Similarly, the methodology implemented and discussed in our analysis may be beneficial for a variety of studies in galaxy formation with alternative dark matter models. That is, our methods can be applicable in constraining characteristics of dark matter halos formed in other dark matter models. For example, dwarf galaxies simulated in self-interacting dark matter have characteristic central densities that are proportional to the interaction cross-section (see Rocha et al. 2013). Preliminary results indicate that cores in self-interacting dark matter halos are “sharper” than those in feedback-affected CDM halos, perhaps indicating a path for differentiating between the two models in the presence of exquisite data (M. Straight et al., in preparation).

Perhaps the most exciting direction for future work will involve direct comparisons and modeling of observational data. In order to enable comparisons with observations, we provide fitting functions for r_c and other profile fit parameters as a function of M_\star/M_{halo} (see Eqs. (12–14) and Tables 1–3). Appendix A provides fits as a function of M_\star . Best fit parameters for all 54 of our galaxies are listed in Table E1. Resulting core-Einasto parameters can be utilized with analytic expressions for the mass profile, gravitational potential, and energy as presented in Appendix B.

We have also shown that the dark matter rotation curves are well-captured by the core-Einasto fits in our simulations in Fig. 6, which motivates a comparison to current rotation curve data, such as the that from the THINGS survey (Walter et al. 2008; Oh et al. 2015) or SPARC (Lelli et al. 2016). For examples of modeling with analytical profiles, we refer to the reader to analysis conducted by, but not limited to, Kamada et al. (2017); Katz et al. (2017); Ren et al. (2019); Kaplinghat et al. (2019); Robles et al. (2019); Li et al. (2020). With the advent of future astrometric data being collected by *Gaia* (Gaia Collaboration et al. 2016b,a, 2018a,b), our model can also be combined with the central density normalizations obtainable in Lazar & Bullock (2020) from the proper motions of dispersion-supported galaxies in order to constrain possible core radii and central densities via Eq. (9).

ACKNOWLEDGEMENTS

We would like to thank the referee for helpful comments on the earlier versions of this article. AL and JSB was supported by the National Science Foundation (NSF) grant AST-1910965. MBK acknowledges support from NSF CAREER award AST-1752913, NSF grant AST-1910346, NASA grant NNX17AG29G, and HST-AR-14282, HST-AR-14554, HST-AR-15006, HST-GO-14191, and HST-GO-15658 from the Space Telescope Science Institute, which is operated by AURA, Inc., under NASA contract NAS5-26555. TKC is supported by STFC astronomy consolidated grant ST/T000244 ASG is supported by the McDonald Observatory at the University of Texas at Austin, through the Harlan J. Smith fellowship. AW received support from NASA through ATP grant 80NSSC18K1097 and HST grants GO-14734, AR-15057, AR-15809, and GO-15902

from STScI; the Heising-Simons Foundation; and a Hellman Fellowship. KE is supported by an NSF graduate research fellowship. Support for CW was provided by NASA through the NASA Hubble Fellowship grant #10938 awarded by STScI. DK acknowledges support from NSF grant AST-1715101 and the Cottrell Scholar Award from the Research Corporation for Science Advancement. Simulations presented in this work utilized resources granted by the Extreme Science and Engineering Discovery Environment (XSEDE), which is supported by National Science Foundation grant no. OCI-1053575. CAFG was supported by NSF through grants AST-1517491, AST-1715216, and CAREER award AST-1652522; by NASA through grant 17-ATP17-0067; and by a Cottrell Scholar Award from the Research Corporation for Science Advancement. The analysis in this paper depended on the python packages NumPy (van der Walt et al. 2011), SciPy (Oliphant 2007), and Matplotlib (Hunter 2007); We are thankful to the developers of these tools. This research has made intensive use of NASA's Astrophysics Data System (<http://ui.adsabs.harvard.edu/>) and the arXiv eprint service (<http://arxiv.org>).

REFERENCES

- Battaglia G., et al., 2005, *MNRAS*, **364**, 433
- Behroozi P. S., Wechsler R. H., Wu H.-Y., 2013, *ApJ*, **762**, 109
- Behroozi P., Wechsler R. H., Hearin A. P., Conroy C., 2019, *MNRAS*, **488**, 3143
- Benítez-Llambay A., Frenk C. S., Ludlow A. D., Navarro J. F., 2019, *MNRAS*, **488**, 2387
- Binney J., Tremaine S., 2008, *Galactic Dynamics: Second Edition*
- Blumenthal G. R., Faber S. M., Flores R., Primack J. R., 1986, *ApJ*, **301**, 27
- Bose S., et al., 2019, *MNRAS*, **486**, 4790
- Boylan-Kolchin M., Bullock J. S., Kaplinghat M., 2011, *MNRAS*, **415**, L40
- Brook C. B., Di Cintio A., 2015, *MNRAS*, **450**, 3920
- Brook C. B., Stinson G., Gibson B. K., Wadsley J., Quinn T., 2012, *MNRAS*, **424**, 1275
- Brooks A. M., Zolotov A., 2014, *ApJ*, **786**, 87
- Bryan G. L., Norman M. L., 1998, *ApJ*, **495**, 80
- Bullock J. S., Boylan-Kolchin M., 2017, *ARA&A*, **55**, 343
- Catena R., Ullio P., 2010, *JCAP*, **2010**, 004
- Chan T. K., Kereš D., Oñorbe J., Hopkins P. F., Muratov A. L., Faucher-Giguère C. A., Quataert E., 2015, *MNRAS*, **454**, 2981
- Chan T. K., Kereš D., Wetzel A., Hopkins P. F., Faucher-Giguère C. A., El-Badry K., Garrison-Kimmel S., Boylan-Kolchin M., 2018, *MNRAS*, **478**, 906
- Cole D. R., Dehnen W., Wilkinson M. I., 2011, *MNRAS*, **416**, 1118
- Deason A. J., Belokurov V., Evans N. W., An J., 2012, *MNRAS*, **424**, L44
- Dekel A., Ishai G., Dutton A. A., Maccio A. V., 2017, *MNRAS*, **468**, 1005
- Di Cintio A., Brook C. B., Maccio A. V., Stinson G. S., Knebe A., Dutton A. A., Wadsley J., 2014a, *MNRAS*, **437**, 415
- Di Cintio A., Brook C. B., Dutton A. A., Maccio A. V., Stinson G. S., Knebe A., 2014b, *MNRAS*, **441**, 2986
- Dubinski J., Carlberg R. G., 1991, *ApJ*, **378**, 496
- Dutton A. A., Maccio A. V., 2014, *MNRAS*, **441**, 3359
- Dutton A. A., Maccio A. V., Buck T., Dixon K. L., Blank M., Obreja A., 2019, *MNRAS*, **486**, 655
- Einasto J., 1965, *Trudy Astrofizicheskogo Instituta Alma-Ata*, **5**, 87
- El-Badry K., Wetzel A., Geha M., Hopkins P. F., Kereš D., Chan T. K., Faucher-Giguère C.-A., 2016, *ApJ*, **820**, 131
- El-Badry K., et al., 2018a, *MNRAS*, **473**, 1930
- El-Badry K., et al., 2018b, *MNRAS*, **480**, 652
- El-Zant A., Shlosman I., Hoffman Y., 2001, *ApJ*, **560**, 636
- Faucher-Giguère C.-A., Lidz A., Zaldarriaga M., Hernquist L., 2009, *ApJ*, **703**, 1416
- Ferland G. J., Korista K. T., Verner D. A., Ferguson J. W., Kingdon J. B., Verner E. M., 1998, *PASP*, **110**, 761
- Fitts A., et al., 2017, *MNRAS*, **471**, 3547
- Flores R. A., Primack J. R., 1994, *ApJ*, **427**, L1
- Freundlich J., et al., 2020, arXiv e-prints, p. arXiv:2004.08395
- Gaia Collaboration et al., 2016a, *A&A*, **595**, A1
- Gaia Collaboration et al., 2016b, *A&A*, **595**, A2
- Gaia Collaboration et al., 2018a, *A&A*, **616**, A1
- Gaia Collaboration et al., 2018b, *A&A*, **616**, A12
- Gao L., Navarro J. F., Cole S., Frenk C. S., White S. D. M., Springel V., Jenkins A., Neto A. F., 2008, *MNRAS*, **387**, 536
- Garrison-Kimmel S., Rocha M., Boylan-Kolchin M., Bullock J. S., Lally J., 2013, *MNRAS*, **433**, 3539
- Garrison-Kimmel S., Boylan-Kolchin M., Bullock J. S., Kirby E. N., 2014, *MNRAS*, **444**, 222
- Garrison-Kimmel S., Bullock J. S., Boylan-Kolchin M., Bardwell E., 2017, *MNRAS*, **464**, 3108
- Garrison-Kimmel S., et al., 2019, *MNRAS*, **487**, 1380
- Gentile G., Salucci P., Klein U., Vergani D., Kalberla P., 2004, *MNRAS*, **351**, 903
- Gnedin O. Y., Kravtsov A. V., Klypin A. A., Nagai D., 2004, *ApJ*, **616**, 16
- Goerdt T., Moore B., Read J. I., Stadel J., 2010, *ApJ*, **725**, 1707
- Governato F., et al., 2010, *Nature*, **463**, 203
- Governato F., et al., 2012, *MNRAS*, **422**, 1231
- Graus A. S., et al., 2019, *MNRAS*, **490**, 1186
- Griffen B. F., Ji A. P., Dooley G. A., Gómez F. A., Vogelsberger M., O'Shea B. W., Frebel A., 2016, *ApJ*, **818**, 10
- Hahn O., Abel T., 2011, *MNRAS*, **415**, 2101
- Hopkins P. F., 2015, *MNRAS*, **450**, 53
- Hopkins P. F., Kereš D., Oñorbe J., Faucher-Giguère C.-A., Quataert E., Murray N., Bullock J. S., 2014, *MNRAS*, **445**, 581
- Hopkins P. F., et al., 2018, *MNRAS*, **480**, 800
- Hunter J. D., 2007, *Computing in Science and Engineering*, **9**, 90
- Kamada A., Kaplinghat M., Pace A. B., Yu H.-B., 2017, *Phys. Rev. Lett.*, **119**, 111102
- Kaplinghat M., Ren T., Yu H.-B., 2019, arXiv e-prints, p. arXiv:1911.00544
- Katz H., Lelli F., McGaugh S. S., Di Cintio A., Brook C. B., Schombert J. M., 2017, *MNRAS*, **466**, 1648

- Klypin A., Yepes G., Gottlöber S., Prada F., Heß S., 2016, *MNRAS*, **457**, 4340
- Kroupa P., 2001, *MNRAS*, **322**, 231
- Lazar A., Bullock J. S., 2020, *MNRAS*, **493**, 5825
- Leitherer C., et al., 1999, *ApJS*, **123**, 3
- Lelli F., McGaugh S. S., Schombert J. M., 2016, *AJ*, **152**, 157
- Li P., Lelli F., McGaugh S., Schombert J., 2020, *ApJS*, **247**, 31
- Ludlow A. D., Navarro J. F., Springel V., Vogelsberger M., Wang J., White S. D. M., Jenkins A., Frenk C. S., 2010, *MNRAS*, **406**, 137
- Ludlow A. D., Bose S., Angulo R. E., Wang L., Hellwing W. A., Navarro J. F., Cole S., Frenk C. S., 2016, *MNRAS*, **460**, 1214
- Macciò A. V., Crespi S., Blank M., Kang X., 2020, *MNRAS*,
- Madau P., Shen S., Governato F., 2014, *ApJ*, **789**, L17
- Mashchenko S., Couchman H. M. P., Wadsley J., 2006, *Nature*, **442**, 539
- Merritt D., Graham A. W., Moore B., Diemand J., Terzić B., 2006, *AJ*, **132**, 2685
- Moore B., 1994, *Nature*, **370**, 629
- Munshi F., et al., 2013, *ApJ*, **766**, 56
- Navarro J. F., Eke V. R., Frenk C. S., 1996, *MNRAS*, **283**, L72
- Navarro J. F., Frenk C. S., White S. D. M., 1997, *ApJ*, **490**, 493
- Navarro J. F., et al., 2004, *MNRAS*, **349**, 1039
- Navarro J. F., et al., 2010, *MNRAS*, **402**, 21
- Nesti F., Salucci P., 2013, *JCAP*, **2013**, 016
- Oñorbe J., Garrison-Kimmel S., Maller A. H., Bullock J. S., Rocha M., Hahn O., 2014, *MNRAS*, **437**, 1894
- Oñorbe J., Boylan-Kolchin M., Bullock J. S., Hopkins P. F., Kereš D., Faucher-Giguère C.-A., Quataert E., Murray N., 2015, *MNRAS*, **454**, 2092
- Oh S.-H., Brook C., Governato F., Brinks E., Mayer L., de Blok W. J. G., Brooks A., Walter F., 2011, *AJ*, **142**, 24
- Oh S.-H., et al., 2015, *AJ*, **149**, 180
- Oliphant T. E., 2007, *Computing in Science and Engineering*, **9**, 10
- Papastergis E., Giovanelli R., Haynes M. P., Shankar F., 2015, *A&A*, **574**, A113
- Peñarrubia J., Pontzen A., Walker M. G., Koposov S. E., 2012, *ApJ*, **759**, L42
- Planck Collaboration et al., 2016, *A&A*, **594**, A13
- Pontzen A., Governato F., 2012, *MNRAS*, **421**, 3464
- Portail M., Gerhard O., Wegg C., Ness M., 2017, *MNRAS*, **465**, 1621
- Power C., Navarro J. F., Jenkins A., Frenk C. S., White S. D. M., Springel V., Stadel J., Quinn T., 2003, *MNRAS*, **338**, 14
- Prada F., Klypin A. A., Simonneau E., Betancort-Rijo J., Paturi S., Gottlöber S., Sanchez-Conde M. A., 2006, *ApJ*, **645**, 1001
- Price D. J., Monaghan J. J., 2007, *MNRAS*, **374**, 1347
- Read J. I., Gilmore G., 2005, *MNRAS*, **356**, 107
- Read J. I., Agertz O., Collins M. L. M., 2016, *MNRAS*, **459**, 2573
- Relatores N. C., et al., 2019, *ApJ*, **887**, 94
- Ren T., Kwa A., Kaplinghat M., Yu H.-B., 2019, *Physical Review X*, **9**, 031020
- Robles V. H., Bullock J. S., Boylan-Kolchin M., 2019, *MNRAS*, **483**, 289
- Rocha M., Peter A. H. G., Bullock J. S., Kaplinghat M., Garrison-Kimmel S., Oñorbe J., Moustakas L. A., 2013, *MNRAS*, **430**, 81
- Romano-Díaz E., Shlosman I., Hoffman Y., Heller C., 2008, *ApJ*, **685**, L105
- Salucci P., Burkert A., 2000, *ApJ*, **537**, L9
- Samuel J., et al., 2020, *MNRAS*, **491**, 1471
- Spekkens K., Giovanelli R., Haynes M. P., 2005, *AJ*, **129**, 2119
- Springel V., 2005, *MNRAS*, **364**, 1105
- Srisawat C., et al., 2013, *MNRAS*, **436**, 150
- Stinson G. S., Bailin J., Couchman H., Wadsley J., Shen S., Nickerson S., Brook C., Quinn T., 2010, *MNRAS*, **408**, 812
- Stinson G. S., et al., 2012, *MNRAS*, **425**, 1270
- Swaters R. A., Madore B. F., van den Bosch F. C., Balcells M., 2003, *ApJ*, **583**, 732
- Teysseier R., Pontzen A., Dubois Y., Read J. I., 2013, *MNRAS*, **429**, 3068
- Tollerud E. J., Boylan-Kolchin M., Bullock J. S., 2014, *MNRAS*, **440**, 3511
- Tollet E., et al., 2016, *MNRAS*, **456**, 3542
- Tonini C., Lapi A., Salucci P., 2006, *ApJ*, **649**, 591
- Walter F., Brinks E., de Blok W. J. G., Bigiel F., Kennicutt Robert C. J., Thornley M. D., Leroy A., 2008, *AJ*, **136**, 2563
- Wang L., Dutton A. A., Stinson G. S., Macciò A. V., Penzo C., Kang X., Keller B. W., Wadsley J., 2015, *MNRAS*, **454**, 83
- Wang J., Bose S., Frenk C. S., Gao L., Jenkins A., Springel V., White S. D. M., 2019, arXiv e-prints, p. arXiv:1911.09720
- Wetzel A. R., Hopkins P. F., Kim J.-h., Faucher-Giguère C.-A., Kereš D., Quataert E., 2016, *ApJ*, **827**, L23
- Wheeler C., et al., 2019, *MNRAS*, **490**, 4447
- Zhao H., 1996, *MNRAS*, **278**, 488
- van der Walt S., Colbert S. C., Varoquaux G., 2011, *Computing in Science and Engineering*, **13**, 22

APPENDIX A: STELLAR MASS PARAMETERIZATION OF THE CORE-EINASTO

The analysis presented in Section 4 focused on properties recovered by the core-Einasto profile and then characterizing these trends with the $M_{\star}/M_{\text{halo}}$ of the simulated FIRE-2 halos. Here, we perform our analysis now on the stellar mass of the galaxies, M_{\star} , as this can provide deeper insight to observations of real galaxies comparable to the galaxies analyzed in this article.

The left plot in Fig. A1 depicts the relation of \tilde{r}_s to r_{-2} of the galaxies' dark matter profile as a function of M_{\star} . We find quite a bit of difference between this implied relationship and the relationship seen previously in Fig. 8. Primarily, the values of \tilde{r}_s/r_{-2} are more spread out for the ranges of M_{\star} considered here. This is better seen with fitting the data with Eq. (13). Best fit results are given in Table 2 and are shown as the blue curve in the left plot. The right plot of Fig. A1 shows the ratio between the concentrations of the

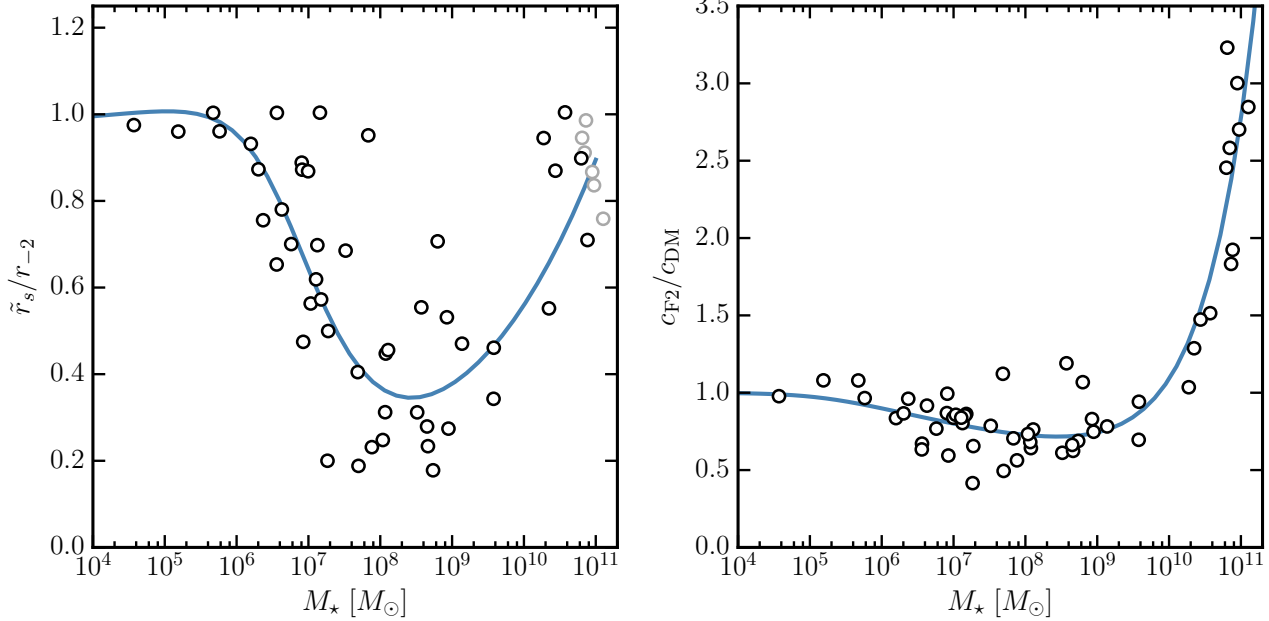


Figure A1. Halo concentration as a function of M_* . *Left:* The ratio of the scale parameter \tilde{r}_s to r_{-2} of the galaxy dark matter profile shows similar trends seen in earlier Fig. 9. The largest difference again correlates with the largest cores at $M_* = 10^{8-9} M_\odot$. The solid blue curve depicts the fit of the points using the best-fit parameters given in Table 2 when using Eq. (13) for $x = M_*$. *Right:* The comparison between concentrations as a function of stellar mass. The reduction of concentration is apparent for a large span of M_* . The solid blue curve depicts the fit of points using best-fit parameters from Table 3 when using Eq. (14) for $x = M_*$.

halos for the galaxies and the DMO analogs. We consider the same definition of the concentration discussed previously in Fig. 9. The depletion in concentration spans from $M_* \simeq 10^6 - 10^9 M_\odot$, the most prominent being at $M_* \simeq 10^{7-8} M_\odot$. The points are fitted with Eq. (14) with the best fit results, given in Table 1, are shown as the blue curve in the right plot.

APPENDIX B: ANALYTICAL PROPERTIES OF CORE-EINASTO HALOS

Here we derive formulae in the form concerning the spatial properties of dark matter halos described by Eq. (8). In the limit of $r_c \rightarrow 0$, profiles should transform back to a cusped form, i.e., $\rho_{c\text{Ein}} \rightarrow \rho_{\text{Ein}}$.

B1 Cumulative mass distribution

For a spherical averaged volume, the cumulative mass is

$$M(< r) = 4\pi\tilde{\rho}_s \int_0^r dr' r'^2 \exp \left\{ -\frac{2}{\alpha_\epsilon} \left[\left(\frac{r' + r_c}{\tilde{r}_s} \right)^{\alpha_\epsilon} - 1 \right] \right\}. \quad (\text{B1})$$

Let us set $s = 2(r + r_c)^{\alpha_\epsilon} / \alpha_\epsilon \tilde{r}_s^{\alpha_\epsilon}$, such that algebraically massaging gives us $r = s^{1/\alpha_\epsilon} (\alpha_\epsilon/2)^{1/\alpha_\epsilon} \tilde{r}_s - r_c$. When substituting this into the cumulative mass expression, we have the

expanded form of

$$M(< r) = \frac{4\pi\tilde{\rho}_s e^{2/\alpha_\epsilon}}{\alpha_\epsilon} \left\{ \tilde{r}_s^3 \left(\frac{\alpha_\epsilon}{2} \right)^{3/\alpha_\epsilon} \int_{s(0)}^{s(r)} ds s^{3/\alpha_\epsilon - 1} e^{-s} \right. \\ + r_c^2 \tilde{r}_s \left(\frac{\alpha_\epsilon}{2} \right)^{1/\alpha_\epsilon} \int_{s(0)}^{s(r)} ds s^{1/\alpha_\epsilon - 1} e^{-s} \\ \left. - 2r_c \tilde{r}_s^2 \left(\frac{\alpha_\epsilon}{2} \right)^{2/\alpha_\epsilon} \int_{s(0)}^{s(r)} ds s^{2/\alpha_\epsilon - 1} e^{-s} \right\}. \quad (\text{B2})$$

We can define the integral parametrization as

$$\tilde{\gamma}_\beta[x_1, x_2] := \left(\frac{\alpha_\epsilon \tilde{r}_s^{\alpha_\epsilon}}{2} \right)^\beta \gamma_\beta[x_1, x_2], \quad (\text{B3})$$

which is a characterization variant of the lower incomplete gamma function:

$$\gamma_\beta[x_1, x_2] = \int_{x_1}^{x_2} ds s^{\beta-1} e^{-s}. \quad (\text{B4})$$

This allows us to write the expression for the integrated mass in a more compact form

$$M(< r) = \frac{4\pi\tilde{\rho}_s e^{2/\alpha_\epsilon}}{\alpha_\epsilon} \left\{ \tilde{\gamma}_{3/\alpha_\epsilon}[s(0), s(r)] + r_c^2 \tilde{\gamma}_{1/\alpha_\epsilon}[s(0), s(r)] \right. \\ \left. - 2r_c \tilde{\gamma}_{2/\alpha_\epsilon}[s(0), s(r)] \right\}. \quad (\text{B5})$$

In the limit of $r_c \rightarrow 0$, we return back to the analytic form of the cumulative mass for the Einasto profile

$$M_{\text{Ein}}(< r) = \lim_{r_c \rightarrow 0} M_{c\text{Ein}}(< r) \\ = \frac{4\pi\tilde{\rho}_s e^{2/\alpha_\epsilon}}{\alpha_\epsilon} \tilde{r}_s^3 \left(\frac{\alpha_\epsilon}{2} \right)^{3/\alpha_\epsilon} \gamma_{3/\alpha_\epsilon}[0, s(r)], \quad (\text{B6})$$

where we then retrieve the lower incomplete gamma function in this limit

$$\gamma_\beta [0, x] = \int_0^x ds s^{\beta-1} e^{-s}. \quad (\text{B7})$$

B2 Gravitational potential

The gravitational potential of a spherically symmetric mass distribution, $\rho(r)$, can be found through the expression (Binney & Tremaine 2008),

$$\Psi(r) = 4\pi G \left[\int_0^r dr' r'^2 \rho(r') + \int_r^\infty dr' r' \rho(r') \right]. \quad (\text{B8})$$

It follows for the cored-Einasto,

$$\Psi(r) = \frac{4\pi G \tilde{\rho}_s e^{2/\alpha_\epsilon}}{\alpha_\epsilon} \left\{ \frac{1}{r} \left(\tilde{\gamma}_{3/\alpha_\epsilon} [s(0), s(r)] \right. \right. \quad (\text{B9})$$

$$\left. \left. + r_c^2 \tilde{\gamma}_{1/\alpha_\epsilon} [s(0), s(r)] - 2r_c \tilde{\gamma}_{2/\alpha_\epsilon} [s(0), s(r)] \right) \right. \\ \left. + \tilde{\Gamma}_{2/\alpha_\epsilon} [s(r)] - r_c \tilde{\Gamma}_{1/\alpha_\epsilon} [s(r)] \right\}, \quad (\text{B10})$$

where we have defined

$$\tilde{\Gamma}_\beta [s(r)] = \left(\frac{\alpha_\epsilon \tilde{r}_s^{\alpha_\epsilon}}{2} \right)^\beta \Gamma_\beta [s(r)], \quad (\text{B11})$$

such that

$$\Gamma_\beta [x] = \int_x^\infty ds s^{\beta-1} s^{-s} \quad (\text{B12})$$

is the upper incomplete Gamma function.

B3 Energy of induced core formation

The transformation from a cusp inner region to a core is presumed to be from highly energetic stellar feedback. After the dark matter cusp is removed we would infer that the halo settles in a new equilibrium state. Dark matter in dynamical equilibrium will then satisfy the virial theorem, i.e. $E = \mathcal{W}/2$. Here, \mathcal{W} is the magnitude of the gravitational potential energy associated with the mass distribution:

$$\mathcal{W} = - \int_0^{r_{\text{vir}}} dr' \frac{GM(< r')}{r'} 4\pi r'^2 \rho(r'). \quad (\text{B13})$$

For the core-Einasto, the gravitational energy is

$$\mathcal{W}_{\text{cEin}} = - \left(\frac{16\pi^2 G^2 \tilde{\rho}_s^2 e^{4/\alpha_\epsilon}}{\alpha_\epsilon} \right) \int_0^{r_{\text{vir}}} dr' e^{-s(r')} \times \quad (\text{B14}) \\ \left\{ \tilde{\gamma}_{3/\alpha_\epsilon} [s(0), s(r')] + r_c^2 \tilde{\gamma}_{1/\alpha_\epsilon} [s(0), s(r')] \right. \\ \left. - 2r_c \tilde{\gamma}_{2/\alpha_\epsilon} [s(0), s(r')] \right\},$$

while for the cusp nature, the Einasto profile has

$$\mathcal{W}_{\text{Ein}} = - \left(\frac{16\pi^2 G^2 \rho_{-2}^2 e^{4/\alpha_\epsilon}}{\alpha_\epsilon} \right) \int_0^{r_{\text{vir}}} dr' \exp \left[\frac{2}{\alpha_\epsilon} \left(\frac{r'}{r_{-2}} \right)^{\alpha_\epsilon} \right] \\ \times \left(\frac{2r_{-2}^2}{\alpha_\epsilon} \right)^{3/\alpha_\epsilon} \gamma_{3/\alpha_\epsilon} \left[0, \frac{2}{\alpha_\epsilon} \left(\frac{r'}{r_{-2}} \right)^{\alpha_\epsilon} \right]. \quad (\text{B15})$$

Table C1. Best-fit parameters for Milky Way-mass halos.

Halo Name	$\tilde{\rho}_s$ [$M_\odot \text{ kpc}^{-3}$]	\tilde{r}_s [kpc]	X	r_c [kpc]	Q_{min}
m12b	1.1×10^6	21.2	5.44	✓1.77	0.0236
m12c	4.4×10^5	31.5	5.50	✓1.52	0.0349
m12f	1.3×10^6	21.3	3.73	✓1.73	0.0230
m12i	2.0×10^6	16.5	2.37	✓1.28	0.0085
m12m	1.0×10^6	22.1	5.50	✓2.31	0.0306
Romeo	2.8×10^6	15.1	3.54	✓0.76	0.0168
Juliet	1.6×10^6	17.2	3.93	✓0.70	0.0187

Note. Use Eq. (C2) with $\alpha_\epsilon = 0.16$.

Analytically, we can then quantify a conservative limit for the lower bound of energy needed to transform the inner density via the virial theorem, i.e.,

$$\Delta E = \frac{\Delta \mathcal{W}}{2} = \frac{\mathcal{W}_{\text{cEin}} - \mathcal{W}_{\text{Ein}}}{2}. \quad (\text{B16})$$

APPENDIX C: A PROFILE FOR BARYONIC CONTRACTED HALOS

A major focus of this work is that Eq. (8), ρ_{cEin} , characterizes dark matter profiles with dark matter cores. While a majority of the dwarf galaxies in our sample are well described by ρ_{cEin} , a majority of our MW-mass halos (not including m12w, m12z, Louise, and Thelma) are not well fitted by this profile given the inaccurate results of r_c . This seems to happen for MW-mass halos that have small cores garnished with baryonic contraction to their dark matter distribution in the innermost regions. This motivates us to come up with a profile that accommodates both of these features in galaxies that are this massive.

We would guess that the amplitude of a baryonic-contracted halo has the density amplitude be radially dependent:

$$\tilde{\rho}_{s,\text{BC}}(r) = \tilde{\rho}_s \left[1 + X \cdot \tanh \left(\frac{r_c}{r} \right) \right], \quad (\text{C1})$$

which contributes to the profile at small radii. Here, X is some free variable in the fit that is added to compensate for unusual amplitudes in several of the MW-mass halos. This is written in a way such that at $r_c = 0$, we only have $\tilde{\rho}_{s,\text{BC}} = \tilde{\rho}_s = \rho_{-2}$, and at $r = 0$, we have $\tilde{\rho}_{s,\text{BC}} = \tilde{\rho}_s(1 + X)$. It would then

$$\rho_{\text{cEin,BC}}(r) = \tilde{\rho}_{s,\text{BC}}(r) \times \exp \left\{ - \frac{2}{\alpha_\epsilon} \left[\left(\frac{r + r_c}{\tilde{r}_s} \right)^{\alpha_\epsilon} - 1 \right] \right\}. \quad (\text{C2})$$

Additionally, this allows us to parameterize the central core density similar to Eq. (9):

$$\rho_{0,\text{BC}} := \rho_{\text{cEin,BC}}(0) = \left[1 + X \right] \rho_0. \quad (\text{C3})$$

Fig. C1 plots the results for fitting $\rho_{\text{cEin,BC}}$ (dashed pink curve) to several of the FIRE-2 MW-mass halos (solid black curve). Also plotted is the DMO analog as the gray curve. The value of r_c predicted by $\rho_{\text{cEin,BC}}$ is highlighted in the same color and pointed to with its r_{vir} normalization. We list our values for these fits in Table C1. We can see that for MW-mass halos with both baryonic contraction and a physical core, $\rho_{\text{cEin,BC}}$, while not particularly succinct, is the most

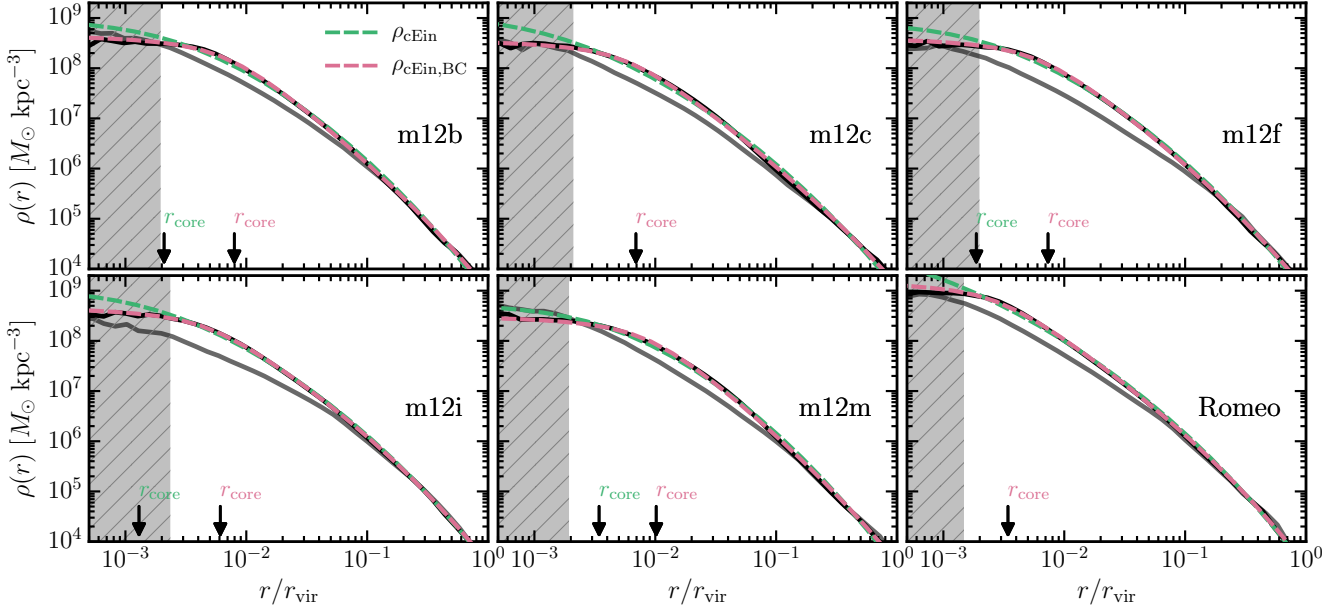


Figure C1. — *Refined profiles for cored MW-mass halos.* As in Fig. 4, galaxies are shown as solid black curves while their DMO analogs are solid grey curves. The original ρ_{cEin} fits are plotted as the green dashed curves while $\rho_{\text{cEin,BC}}$ fits are plotted as the pink dashed curves. The location of the resulting core radius of each galaxy from both fits is indicated by an arrow with the corresponding color. We see that a radially dependent density component in $\rho_{\text{cEin,BC}}$ greatly improves the fits while also accurately predicting the core radius.

ideal function we can use to probe r_c . However, the exact behaviour and physical interpretation of \tilde{r}_s is left, now, somewhat ambiguous compared to how it was expected to behave previously in Section 4. The same MW-mass halos that have had their core radii previously predicted with ρ_{cEin} are also plotted in Fig. C1 as the green dashed curve. The predicted core radius from this profile is pointed to and highlighted in green. From direct comparison between the analytical fits, we see significant improvements. We have included r_c values here in the main text as cyan points in Figs. 7 and 8.

APPENDIX D: COMPARISON WITH OTHER DARK MATTER PROFILES

Here we compare several other dark matter profiles in the literature and compare their fits to our FIRE-2 simulation sample:

- **P12** (Peñarrubia et al. 2012): One commonly adopted dark matter profile that is an extension of the two-parameter NFW profile that accommodates a physical core radius:

$$\rho_{\text{P12}}(r) = \frac{\rho_0 r_0^3}{(r_c + r)(r_0 + r)^2}, \quad (\text{D1})$$

where ρ_0 is the characteristic scale density and r_0 is some scale radius. The form of Eq. (D1) transforms back to a NFW profile in the limit of $r_c \rightarrow 0$. The form of Eq. (D1) is a three-parameter profile with free variables ρ_0 , r_0 , and r_c . Eq. (D1) is fitted with the FIRE-2 halos by utilizing the fitting routine discussed in Section 4 and best-fit parameters are obtained by minimizing the figure-of-merit, Eq. (11).

- **$\alpha\beta\gamma$** (Zhao 1996): A generic five parameter profile dubbed the “ $\alpha\beta\gamma$ -profile”:

$$\rho_{\alpha\beta\gamma}(r) = \frac{\rho_s}{(r/r_s)^{\gamma_s} [1 + (r/r_s)^{\alpha_s}]^{(\beta_s - \gamma_s)/\alpha_s}}, \quad (\text{D2})$$

where r_s is the scale radius and ρ_s is the scale density. The inner and outer regions are parameterized, respectively, by the logarithmic slopes, $-\gamma_s$ and $-\beta_s$, while α_s controls the rate of transition from the inner and outer region. The form of Eq. (D2) has five free-parameters ρ_s , r_s , α_s , β_s , and γ_s . Eq. (D2) is fitted with the FIRE-2 halos by utilizing the routine discussed in Section 4 and best-fit parameters are obtained by minimizing the figure-of-merit, Eq. (11).

- **DC14** (Di Cintio et al. 2014b): The DC14 model takes the generalized form of Eq. (D2) and imposes dependence of the slope parameters as a function of M_\star/M_{halo} :

$$\alpha_s(X) = 2.94 - \log_{10} \left[(10^{X+2.33})^{-1.08} + (10^{X+2.33})^{2.29} \right] \quad (\text{D3})$$

$$\beta_s(X) = 4.23 + 1.34X + 0.26X^2 \quad (\text{D4})$$

$$\gamma_s(X) = -0.06 + \log_{10} \left[(10^{X+2.56})^{-0.68} + (10^{X+2.56}) \right], \quad (\text{D5})$$

where $X := \log_{10}(M_\star/M_{\text{halo}})$ and is valid in the range of $-4.1 < X < -1.3$. Outside this mass range resorts to a NFW profile, i.e., $(\alpha_s, \beta_s, \gamma_s) = (1, 3, 1)$. This now leaves Eq. (D2) with two free-parameters: r_s and ρ_s . The DC14 profile is fitted with the FIRE-2 halos by utilizing the routine discussed in Section 4 and best-fit parameters are obtained by minimizing the figure-of-merit, Eq. (11).

- **DF20** (Dekel et al. 2017; Freundlich et al. 2020): The DF20 model (or the “Dekel+” profile) takes the generic double power-law density profile, namely Eq. (D2), and has fixed

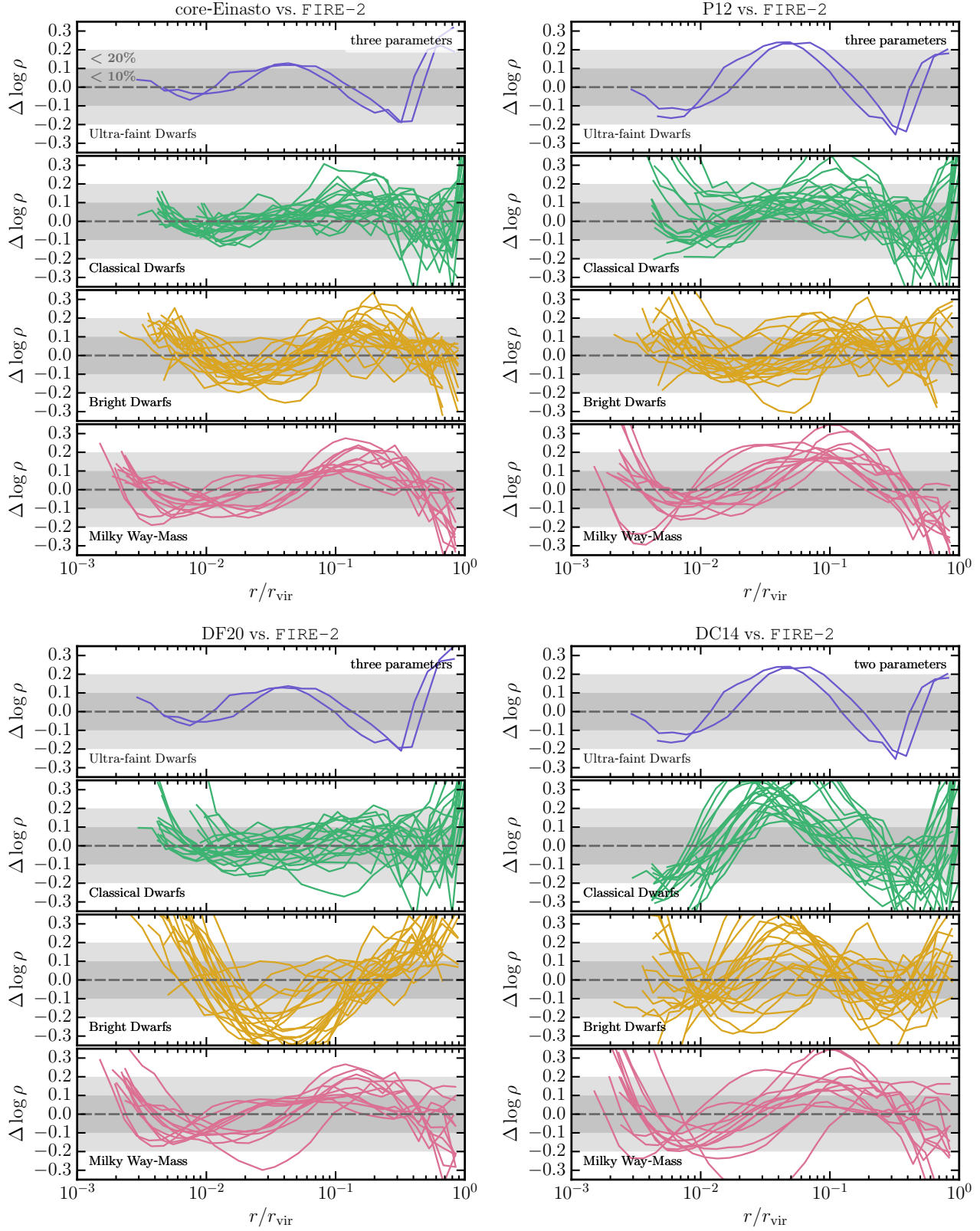


Figure D1. Fit residuals, as in Fig. 5: residuals for core-Einasto (top left), P12 (top right), DF20 (bottom left), and DC14 (bottom right) profiles for our halo sample. The number of free parameters in each fit is indicated in the upper right of each panel. See D for the definition of P12, DF20, and DC14.

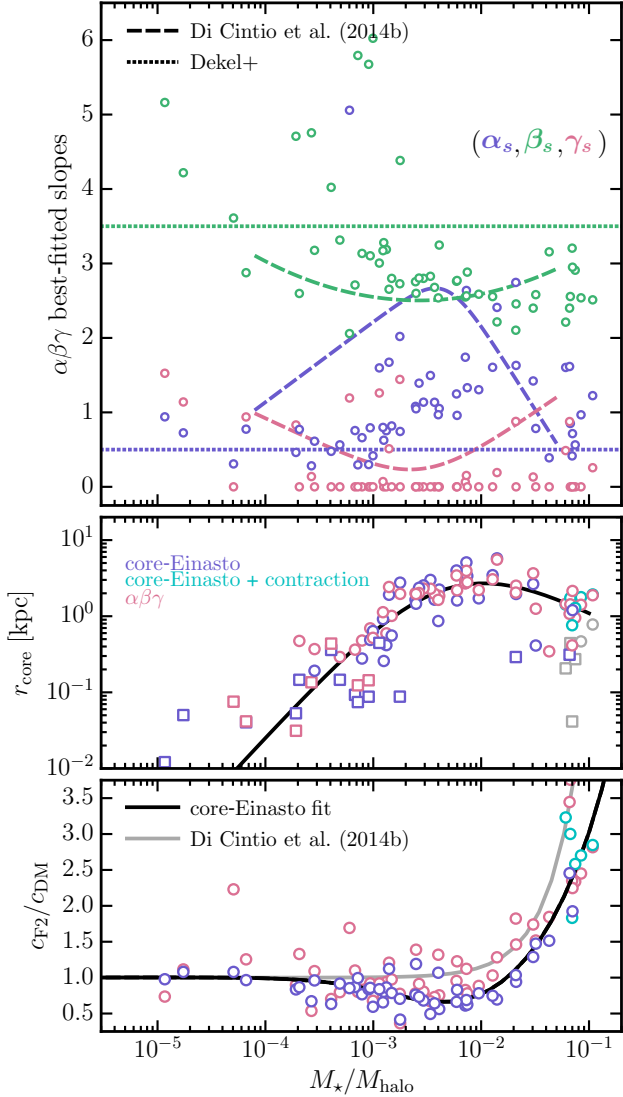


Figure D2. Properties from the $\alpha\beta\gamma$ -profile fits. *Top panel:* The best fitting results for the inner slope (γ_s ; pink), the outer slope (β_s ; green), and the transitioning slope (α_s ; blue). *Middle panel:* The core radius as parameterized from the characteristic radius, r_{-1} , from the best-fit $\alpha\beta\gamma$ -profiles via Eq. (D6). We assumed that r_{-1} acts as a probe of r_c and find agreeable results from r_c derived by fitting Eq. (8) in the main text. *Bottom panel:* The ratio between the concentration parameter for the FIRE-2 halos and their DMO analogs using Eq. (D7). Shown are the core-Einasto (blue) and core-Einasto with contraction (cyan) values presented previously in Fig. 10. Both the FIRE-2 halos and DMO analogs are fitted with the $\alpha\beta\gamma$ -profile to obtain the concentration parameters shown in pink. The concentration ratio is mostly in agreement with slight differences at the edge of the bright dwarf regime ($M_*/M_{\text{halo}} \approx 10^{-2}$).

slopes $\alpha_s = 0.5$ and $\beta_s = 3.5$. This reduces the analytical profile to be fitted based on three free-parameters: ρ_s , r_s , and γ_s . The form of DF20 is fitted with the FIRE-2 halos by utilizing the routine discussed in Section 4 and best-fit parameters are obtained by minimizing the figure-of-merit, Eq. (11).

We also attempted a similar analysis using the core pro-

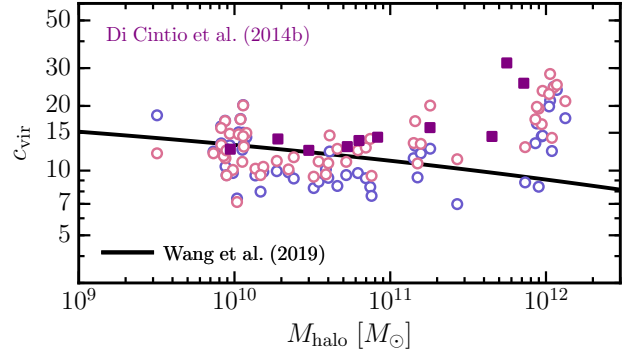


Figure D3. Concentration as a function of dark matter halo mass. Concentration implied from the core-Einasto profile are given by the blue points while the concentration shown from $\alpha\beta\gamma$ -profile fits, i.e., using Eq. (D7), is given in pink. The solid black curve is the concentration relation from Wang et al. (2019). The purple squares are the results taken from Di Cintio et al. (2014b).

file from Read et al. (2016) with their four free-parameters and found the resulting fits incompatible with our simulated profiles.

D1 Resulting profile residuals

Fig. D1 compares the residuals of the FIRE-2 dark matter halos when fitted with the core-Einasto (top left, same fits as presented in the main text), P12 (top right), DF20 (bottom left), and the $\alpha\beta\gamma$ model with DC14 parametrization (bottom right). The interesting comparison to be made is between core-Einasto and P12 since both profiles have three-parameters to be determined, with one being the core radius of the dark matter halo. We see the the core-Einasto does better at fitting the FIRE-2 dark matter halos than the P12 shape. Although, while P12 does not do as well as fitting to our FIRE-2 halos, the form P12 has the advantage of being more analytically friendly when quantifying characteristics of the dark matter halo. For the DF20 model, we find that it is comparable with the core-Einasto fits for the classifications of the ultra-faints, classical dwarfs, and most MW halos. However, DF20 fails to capture the shape of our bright galaxies, i.e., the halos with the largest feedback-induced cores.

Results for the two-parameter DC14 model are shown to be poor fits with the FIRE-2 halos for all of our mass range. This likely has to do with differences in the dark matter distribution found at fixed stellar mass fractions compared to the simulations explored in DC14.

D2 Extended analysis with $\alpha\beta\gamma$

Unsurprisingly, the five-parameter $\alpha\beta\gamma$ model provides a superior fit for a majority of our simulated halos compared to our three-parameter core-Einasto profile. Specifically we find that this profile can do better than 10% for almost all of our galaxies. While the resulting $\alpha\beta\gamma$ -profile fits model the dark matter distribution well, the physical interpretation of the resulting best-fit parameters is less clear. A majority of the fits favor a inner-slope of $\gamma_s = 0$ for several cusped profiles,

which at times imposes too large of a scale radius to be determined (m10d, m10i, and m10j to name a few). Regardless of the physical interpretation of the resulting parameter fits, we find excellent accuracy modeling our halos, which still enables us to extract characteristics of the best-fit profiles. In the next section, we perform a brief analysis on the best-fit parameters for the $\alpha\beta\gamma$ -profile.

In Fig. D2, we present the results when using the $\alpha\beta\gamma$ -profile as function of the stellar mass fraction, M_\star/M_{halo} . The best-fit parameter fits the $\alpha\beta\gamma$ are also presented for each of our halos in Fig. E2.

D2.1 Best-fit slopes

The top panel shows the best fitting results for the inner slope (γ_s ; pink), the outer slope (β_s ; green), and the transitioning slope (α_s ; blue). Also plotted are the trend of the slopes from Di Cintio et al. (2014a) as dashed curves and the dotted curves are having the fixed slopes, $\alpha_s = 0.5$ and $\beta_s = 3.5$, as suggest by Dekel et al. (2017) and Freundlich et al. (2020). Noticeably, the inner-slope, α_s , tends to chooses to be zero as a best-fit parameter for a majority of our galaxies. For β_s and γ_s , a sufficient amount of scatter is seen from the due to allowed large number free-parameters allowed to be fit. Although, trends as a function of M_\star/M_{halo} , can be somewhat made out.

D2.2 Core radius parametrization

Notice that in Fig. 3, the log-slope profile tends to rise at around $d \log \rho / d \log r \approx -1$, which happens at the radius r_{-1} . To play with the idea that the physical core radius can be parameterized by the $\alpha\beta\gamma$ -profile, we see how r_{-1} is able to probe the core radius, i.e.,

$$r_c \approx r_{-1} = \left(\frac{1 - \gamma_s}{\beta_s - 1} \right)^{1/\alpha_s} r_s. \quad (\text{D6})$$

In the middle panel of Fig D2, we plot the previous core radius results from Fig. 7 for core-Einasto (blue points), the baryonic contracted core-Einasto (cyan points), and the median fit (black curve) while also included the $\alpha\beta\gamma$ -profile results using the assumed relation from Eq. (D6). We see that the r_c parametrization from the $\alpha\beta\gamma$ -profile follows the median r_c curve from core-Einasto parametrization extremely well, implying both excellent agreement with our fitted r_c results from core-Einasto and how r_{-1} characterizes the core radius.

D2.3 Halo concentration

Presented in the bottom panel of Fig D2 is the ratio between the concentration parameter of the FIRE-2 halos and their DMO analogs. As noted in Di Cintio et al. (2014b), the radius at which the log-slope of the generic five-parameter profile is equal to -2 , r_{-2} , is mapped from the free-parameters via

$$r_{-2} = \left(\frac{2 - \gamma_s}{\beta_s - 2} \right)^{1/\alpha_s} r_s. \quad (\text{D7})$$

Shown are the points of the core-Einasto (blue) and core-Einasto with contraction (cyan), which are the same values

depicted in Fig. 10 of the main text, while the pink points are the concentration parameters, which is still defined as $c_{\text{vir}} = r_{\text{vir}}/r_{-2}$, for the best-fit $\alpha\beta\gamma$ -profiles. Note that both the FIRE-2 halos and the DMO halos are fitted with $\alpha\beta\gamma$ -profile to quantify the r_{-2} values. We mostly find agreement with either methods of quantifying the halo concentration, though several of the halos in the stellar mass fraction range of $10^{-5} - 10^{-3}$ are strongly scattered. In the classical dwarf regime, we find halos that are less concentrated like we found from the core-Einasto model. We somewhat find agreement in the bright dwarf regime, although a sufficient of scatter is present. Though recently, Freundlich et al. (2020) reports a similar result at this stellar mass fraction. The MW halos are mostly consistent with our previous findings in the main text.

A different viewed of the concentration parameter can be made by taking the previous points and plotting as a function of M_{halo} in Fig. D3. The purple squares are the halos presented in Di Cintio et al. (2014b).

APPENDIX E: SIMULATION SAMPLE

Presented in Tables E1 and E2 are the suite of halos simulated using FIRE-2 with their relevant parameters listed at $z = 0$.

E1 Global and simulation properties

Presented in Table E1 are the global properties of the FIRE-2 galaxies at $z = 0$ as well as the relevant simulation properties. Columns (1-5) contain global properties of the galaxies while columns (6-10) describe the numerical resolution properties of the simulations. All simulations were ran using with $n_{\text{crit}} = 1000$, the minimum gas density required for star formation in addition to self-shielding, Jeans instability, and self-gravity. *References*, given in the last column, are labeled as such — A: Fitts et al. (2017), B: Graus et al. (2019), C: Wheeler et al. (2019), D: Chan et al. (2018), E: El-Badry et al. (2018a), F: Hopkins et al. (2018), G: Garrison-Kimmel et al. (2019), H: Samuel et al. (2020), I: Wetzel et al. (2016). The individual columns in Table E1 are described as follows:

- (1) M_{halo} : The mass of the target halo at $z = 0$ defined by Bryan & Norman (1998).
- (2) r_{vir} : The virial radius in physical units of the target halo.
- (3) V_{max} : The maximum circular velocity curve for the dark matter component of the FIRE-2 dark matter halos, i.e., $V_{\text{max}} := \max[V_{\text{circ}}]$.
- (4) M_\star : Stellar mass (within 10% of r_{vir}) of the central galaxy in the target halo.
- (5) $r_{1/2}$: The physical radius that encloses half the value of M_\star for the central galaxy.
- (6) m_b : The mass of baryon particles of the simulation.
- (7) m_{dm} : The mass of dark matter particles of the simulation.
- (8) ϵ_{dm} : The dark matter force softening
- (9) r_{conv} : Radius of numerical convergence of the DMO analogs, set by Eq. (1) and the most conservative criterion as discussed in Hopkins et al. (2018).

E2 Resulting analytical profile fits

Presented in Table E2 are the best-fit parameters for the core-Einasto and $\alpha\eta\gamma$ -profile. Columns (1-5) are the results of fitting the simulated density profiles to the core-Einasto profile with $\alpha_\epsilon = 0.16$. Columns (6-9) are the results of fitting the simulated density profiles to the $\alpha\beta\gamma$ -profile. The individual columns in Table E2 are described as follows:

(1) $\tilde{\rho}_s$: The scale density fitted as a free parameter for the core-Einasto profile, Eq. (8).

(2) \tilde{r}_s : The scale radius fitted as a free parameter for the core-Einasto profile, Eq. (8).

(3) r_c : The physical core radius of the dark matter profile fitted as a free parameter for the core-Einasto profile, Eq. (8).

(4) $Q_{\min, \text{cEin}}$: The quoted goodness-of-fit parameter for the core-Einasto fit, i.e., Eq. (11).

(5) ρ_s : The scale density fitted as a free parameter for the $\alpha\beta\gamma$ -profile.

(7-9) (α, β, γ) : The three characteristic slopes fitted as a free parameter for the $\alpha\beta\gamma$ -profile.

(10) $Q_{\min, \alpha\beta\gamma}$: The quoted goodness-of-fit parameter for the $\alpha\beta\gamma$ -profile fit, i.e., Eq. (11).

For the quoted core radii (column 3 in Table E2), the symbols are defined as follows: (✓) – Verified location of dark matter core in the simulated profile; (✗) – Improper value of dark matter core in the simulated profile if one is physically present; (†) – Dark matter core radius fitted inside the region of conservative numerical convergence, i.e., $r_c < r_{\text{conv}}$. The exact meaning of these results are discussed in more properly in Section 4.4.

This paper has been typeset from a T_EX/ L^AT_EX file prepared by the author.

Table E1. Global parameters of the FIRE-2 halos.

Halo Name	M_{halo} [M_{\odot}]	r_{vir} [kpc]	V_{max} [km s^{-1}]	M_{\star} [M_{\odot}]	$r_{1/2}$ [kpc]	m_{b} [M_{\odot}]	m_{dm} [M_{\odot}]	ϵ_{dm} [pc]	r_{conv} [kpc]	Reference
(1)	(2)	(3)	(4)	(5)	(6)	(7)	(8)	(9)		
<i>Ultra-Faint Dwarfs (2)</i>										
m10v250	8.9×10^9	57.7	30	1.5×10^5	0.35	250	1300	29	0.166	C
m10v250B	3.2×10^9	40.9	24	3.7×10^4	0.42	250	1300	29	0.153	C
<i>Classical Dwarfs (20)</i>										
m10b	9.3×10^9	54.8	31	4.7×10^5	0.34	500	2500	50	0.218	A
m10c	8.8×10^9	54.1	31	5.8×10^5	0.35	500	2500	50	0.227	A
m10d	8.2×10^9	50.7	32	1.6×10^6	0.53	500	2500	50	0.209	A
m10e	9.8×10^9	53.8	31	2.0×10^6	0.62	500	2500	50	0.216	A
m10f	8.7×10^9	51.5	35	4.7×10^6	0.75	500	2500	50	0.202	A
m10g	7.3×10^9	48.6	32	5.7×10^6	0.95	500	2500	50	0.215	A
m10h	1.2×10^{10}	57.2	37	8.1×10^6	0.83	500	2500	50	0.207	A
m10i	1.1×10^{10}	56.3	40	8.2×10^6	0.57	500	2500	50	0.195	A
m10j	1.1×10^{10}	55.4	37	9.9×10^6	0.70	500	2500	50	0.194	A
m10k	1.1×10^{10}	56.4	38	1.1×10^7	1.14	500	2500	50	0.207	A
m10l	1.1×10^{10}	56.1	37	1.3×10^7	0.78	500	2500	50	0.202	A
m10m	1.1×10^{10}	56.1	38	1.5×10^7	0.96	500	2500	50	0.208	A
m10q250	8.2×10^9	56.2	33	2.3×10^6	0.81	250	1300	29	0.150	C
m10xc _A	8.5×10^9	53.1	35	8.5×10^6	1.80	4000	20000	100	0.455	B
m10xd _A	2.4×10^{10}	75.5	38	1.4×10^7	1.90	4000	20000	100	0.476	B
m10xe _A	1.4×10^{10}	62.5	35	3.6×10^6	1.27	4000	20000	100	0.529	B
m10xe _B	1.1×10^{10}	58.6	38	1.3×10^7	1.90	4000	20000	100	0.488	B
m10xe _C	1.0×10^{10}	57.0	34	1.8×10^7	3.00	4000	20000	100	0.474	B
m10xe _D	8.9×10^9	53.9	34	3.6×10^6	1.47	4000	20000	100	0.482	B
m10xg _A	1.5×10^{10}	64.4	40	1.9×10^7	2.20	4000	20000	100	0.465	B
<i>Bright Dwarfs (20)</i>										
m10xa	1.9×10^{10}	69.4	45	7.6×10^7	3.18	4000	20000	100	0.453	B
m10xb	2.2×10^{10}	73.5	42	3.3×10^7	2.39	4000	20000	100	0.480	B
m10xc	3.2×10^{10}	82.9	48	1.2×10^8	3.26	4000	20000	100	0.451	B
m10xd	3.9×10^{10}	88.5	53	6.8×10^7	4.04	4000	20000	100	0.437	B
m10xe	4.5×10^{10}	93.6	56	3.3×10^8	4.17	4000	20000	100	0.448	B
m10xf	5.2×10^{10}	97.7	58	1.3×10^8	3.33	4000	20000	100	0.453	B
m10xg	6.2×10^{10}	103	65	4.6×10^8	3.98	4000	20000	100	0.443	B
m10xh	7.4×10^{10}	110	68	5.4×10^8	6.04	4000	20000	100	0.434	B
m10xh _A	1.5×10^{10}	63.9	38	5.0×10^7	3.14	4000	20000	100	0.464	B
m10xi	7.6×10^{10}	111	64	4.5×10^8	5.16	4000	20000	100	0.441	B
m10z	3.5×10^{10}	90.5	49	4.9×10^7	3.20	2100	10000	43	0.370	D
m11a	4.0×10^{10}	95.0	52	1.2×10^8	2.63	2100	10000	43	0.314	D
m11b	4.1×10^{10}	95.6	59	1.1×10^8	2.39	2100	10000	43	0.314	D
m11c	1.4×10^{11}	145	80	8.5×10^8	2.78	2100	10000	43	0.673	F
m11d	2.7×10^{11}	179	88	3.8×10^9	6.01	7100	35000	40	0.502	E
m11e	1.4×10^{11}	146	83	1.4×10^9	3.36	7100	35000	40	0.481	E
m11h	1.8×10^{11}	157	90	3.8×10^9	3.92	7100	35000	40	0.503	E
m11i	7.0×10^{10}	114	62	8.9×10^8	3.35	7100	35000	40	0.548	E
m11q	1.6×10^{11}	153	80	6.3×10^8	2.35	7100	35000	40	0.523	D
m11q880	1.5×10^{11}	114	80	3.7×10^8	2.83	880	4400	20	0.225	E
<i>Milky Way-Mass (12)</i>										
m12b	1.1×10^{12}	224	183	9.4×10^{10}	2.66	7100	35000	40	0.437	G
m12c	1.1×10^{12}	219	157	6.5×10^{10}	3.37	7100	35000	40	0.461	G
m12f	1.3×10^{12}	237	184	8.9×10^{10}	3.60	7100	35000	40	0.471	F
m12i	9.4×10^{11}	210	162	7.0×10^{10}	2.80	7100	35000	40	0.496	I
m12m	1.2×10^{12}	227	187	1.3×10^{11}	4.88	7100	35000	40	0.439	F
m12r	9.0×10^{11}	211	136	1.9×10^{10}	4.37	7100	35000	40	0.476	H
m12w	9.5×10^{11}	215	157	5.5×10^{10}	3.04	7100	35000	40	0.507	H
m12z	7.3×10^{11}	195	130	2.2×10^{10}	4.71	4200	22000	33	0.383	G
Thelma	1.1×10^{12}	220	178	7.7×10^{10}	4.36	4000	20000	32	0.366	G
Louise	8.5×10^{11}	203	159	2.7×10^{10}	3.27	4000	20000	32	0.359	G
Romeo	1.0×10^{12}	222	188	7.3×10^{10}	4.18	3500	20000	31	0.329	G
Juliet	8.7×10^{11}	209	164	3.7×10^{10}	2.14	3500	20000	31	0.339	G

Table E2. Resulting profile fits.

Halo Name	$\tilde{\rho}_s$ [$M_\odot \text{ kpc}^{-3}$]	\tilde{r}_s [kpc]	r_c [kpc]	Q_{\min} cEin	ρ_s [$M_\odot \text{ kpc}^{-3}$]	r_s [kpc]	α_s	β_s	γ_s	Q_{\min} $\alpha\beta\gamma$
(1)	(2)	(3)	(4)	(5)	(6)	(7)	(8)	(9)	(10)	
Ultra-Faint Dwarfs (2)										
m10v250	5.5×10^5	5.82	$\dagger 0.05$	0.0480	3.9×10^5	25.0	0.73	4.22	1.14	0.0462
m10v250B	2.7×10^6	2.21	$\dagger 0.01$	0.0453	9.32×10^4	25.0	0.94	5.16	1.53	0.0328
Classical Dwarfs (20)										
m10b	1.4×10^6	4.02	0.00	0.0414	2.4×10^{10}	1.70	0.31	3.61	0.00	0.0313
m10c	9.4×10^5	4.75	$\dagger 0.04$	0.0398	1.0×10^7	3.44	0.78	2.88	0.93	0.0384
m10d	1.9×10^6	3.53	$\dagger 0.05$	0.0317	6.2×10^6	25.0	0.46	4.71	0.83	0.0328
m10e	1.0×10^6	4.82	$\dagger 0.15$	0.0336	1.8×10^8	0.87	0.77	2.60	0.00	0.0232
m10f	5.6×10^6	2.35	$\dagger 0.15$	0.0575	8.8×10^8	1.29	0.56	3.31	0.00	0.0596
m10g	3.6×10^6	2.78	$\checkmark 0.28$	0.0429	2.3×10^8	1.51	0.66	3.13	0.00	0.0448
m10h	2.7×10^6	3.55	$\dagger 0.10$	0.0418	4.7×10^8	0.74	0.76	2.71	0.00	0.0283
m10i	6.1×10^6	2.43	$\dagger 0.07$	0.0465	1.7×10^{10}	25.0	0.30	5.79	0.00	0.0483
m10j	4.6×10^6	2.77	$\dagger 0.10$	0.0260	1.2×10^{10}	25.0	0.30	5.67	0.00	0.0296
m10k	7.8×10^6	2.39	$\checkmark 0.49$	0.0360	1.4×10^{10}	1.77	0.79	3.10	0.00	0.0363
m10l	5.8×10^6	2.54	$\checkmark 0.26$	0.0360	4.0×10^8	1.63	0.63	3.28	0.00	0.0365
m10m	1.0×10^7	2.14	$\checkmark 0.42$	0.0421	2.1×10^8	1.68	0.75	3.19	0.00	0.0465
m10q250	4.0×10^6	2.64	$\checkmark 0.19$	0.0262	4.4×10^8	1.32	0.61	3.18	0.00	0.0224
m10xcA	1.1×10^7	1.99	$\checkmark 0.64$	0.0262	4.4×10^8	25.0	0.42	6.02	0.00	0.0259
m10xdA	5.3×10^5	8.25	0.00	0.0734	1.3×10^7	1.56	5.06	2.06	1.19	0.0186
m10xeA	6.2×10^5	6.60	0.00	0.0413	2.7×10^9	25.0	0.28	4.75	0.14	0.0422
m10xeB	4.6×10^6	2.90	$\dagger 0.45$	0.0278	1.6×10^6	6.46	1.60	3.01	1.26	0.0186
m10xec	4.1×10^7	1.54	$\checkmark 2.80$	0.0196	1.5×10^7	10.1	0.74	4.38	0.00	0.0187
m10xep	4.1×10^6	2.80	$\dagger 0.36$	0.0601	4.6×10^8	4.45	0.48	4.02	0.00	0.0618
m10xgA	4.0×10^6	3.26	$\checkmark 0.92$	0.0222	4.3×10^7	3.27	0.80	3.17	0.07	0.0194
Bright Dwarfs (20)										
m10xa	5.4×10^7	1.62	$\checkmark 2.24$	0.0240	2.4×10^7	3.99	1.05	3.25	0.00	0.0180
m10xb	1.9×10^6	5.13	$\checkmark 0.56$	0.0248	7.5×10^7	2.07	0.81	2.80	0.00	0.0224
m10xc	4.3×10^6	4.47	$\checkmark 1.65$	0.0346	2.1×10^7	3.10	1.14	2.68	0.00	0.0276
m10xd	8.3×10^5	8.30	$\dagger 0.09$	0.0325	8.1×10^5	10.9	2.02	2.73	1.44	0.0210
m10xe	1.4×10^7	3.32	$\checkmark 2.77$	0.0586	1.2×10^{10}	3.61	1.74	2.55	0.06	0.0206
m10xf	5.7×10^6	4.67	$\checkmark 1.65$	0.0334	3.1×10^9	3.37	1.08	2.75	0.00	0.0268
m10xg	5.1×10^7	2.48	$\checkmark 3.38$	0.0453	2.0×10^7	4.50	1.33	2.88	0.00	0.0304
m10xh	8.7×10^7	2.33	$\checkmark 5.09$	0.0740	7.8×10^6	4.98	2.64	2.57	0.15	0.0174
m10xhA	6.2×10^7	1.51	$\checkmark 3.00$	0.0433	9.8×10^6	3.43	1.49	2.82	0.00	0.0205
m10xi	1.5×10^7	4.05	$\checkmark 3.99$	0.0389	1.2×10^7	5.40	1.25	2.76	0.00	0.0297
m10z	5.6×10^6	4.13	$\checkmark 1.91$	0.0315	5.0×10^6	5.01	1.67	2.65	0.51	0.0206
m11a	1.4×10^7	3.20	$\checkmark 2.54$	0.0286	1.9×10^7	3.91	1.14	2.80	0.00	0.0200
m11b	6.2×10^7	1.93	$\checkmark 2.36$	0.0426	2.9×10^7	3.08	1.39	2.80	0.00	0.0100
m11c	4.6×10^6	6.73	$\checkmark 1.61$	0.0271	5.1×10^7	3.98	0.96	2.77	0.00	0.0254
m11d	5.1×10^6	8.81	$\checkmark 5.75$	0.0594	5.5×10^6	6.56	2.41	2.21	0.19	0.0195
m11e	8.9×10^6	5.26	$\checkmark 1.72$	0.0546	4.6×10^7	3.15	1.30	2.58	0.00	0.0399
m11h	9.3×10^6	5.73	$\checkmark 1.96$	0.0562	3.9×10^7	3.17	1.63	2.46	0.00	0.0169
m11i	2.0×10^7	3.40	$\checkmark 3.46$	0.0495	1.3×10^7	4.02	1.60	2.56	0.00	0.0244
m11q	2.1×10^6	8.97	$\checkmark 0.86$	0.0463	8.3×10^7	2.56	0.97	2.54	0.00	0.0465
m11q880	4.5×10^6	6.81	$\checkmark 1.46$	0.0336	6.0×10^7	3.07	1.05	2.60	0.00	0.0265
Milky Way-Mass (12)										
m12b	6.5×10^6	11.18	$\times 0.47$	0.0528	5.8×10^8	2.21	0.97	2.54	0.00	0.0236
m12c	2.1×10^6	17.14	$\times 0.21$	0.0690	1.3×10^9	2.48	1.60	2.21	0.48	0.0124
m12f	4.3×10^6	13.76	$\times 0.44$	0.0450	6.1×10^8	2.41	0.85	2.56	0.00	0.0224
m12i	3.3×10^6	13.60	$\times 0.27$	0.0255	1.6×10^9	3.00	0.56	2.91	0.00	0.0201
m12m	7.3×10^6	10.96	$\times 0.78$	0.0539	1.8×10^8	3.37	1.22	2.51	0.25	0.0128
m12r	8.1×10^5	23.74	$\dagger 0.29$	0.0611	2.2×10^7	4.56	2.75	2.10	0.88	0.0184
m12w	3.2×10^6	13.31	$\dagger 0.31$	0.0451	4.0×10^7	4.84	1.61	2.40	0.87	0.0222
m12z	3.7×10^6	12.19	$\checkmark 2.64$	0.0432	2.1×10^7	5.12	1.42	2.40	0.13	0.007
Thelma	5.0×10^6	12.66	$\checkmark 1.20$	0.0212	3.0×10^8	5.46	0.71	2.95	0.00	0.026
Louise	3.4×10^6	13.15	$\checkmark 0.41$	0.0371	6.0×10^8	2.25	0.78	2.58	0.00	0.0222
Romeo	5.6×10^6	11.59	$\times 0.04$	0.0400	1.6×10^{10}	2.78	0.42	3.21	0.00	0.0332
Juliet	3.6×10^6	12.70	$\times 0.00$	0.0433	1.8×10^8	2.48	0.39	3.16	0.00	0.0338